Radiative Heating of Large Meteoroids During Atmospheric Entry

Christopher O. Johnston[a,*], Eric C. Stern[b], Lorien F. Wheeler[c]

[a] *NASA Langley Research Center, Hampton, VA 23681*
[b] *NASA Ames Research Center, Moffett Field, CA 94035*
[c] *CSRA, NASA Ames Research Center, Moffett Field, CA 94035*

Abstract

A high-fidelity approach for simulating the aerothermodynamic environments of meteor entries was developed, which allows the commonly assumed heat transfer coefficient of 0.1 to be assessed. This model uses chemically reacting computational fluid dynamics (CFD), coupled with radiation transport and surface ablation. Coupled radiation accounts for the impact of radiation on the flowfield energy equations, while coupled ablation explicitly models the injection of ablation products within the flowfield and radiation simulations. For a meteoroid with a velocity of 20 km/s, coupled radiation is shown to reduce the stagnation point radiative heating by over 60%. The impact of coupled ablation (with coupled radiation) is shown to provide at least a 70% reduction in the radiative heating relative to cases with only coupled radiation. This large reduction is partially the result of the low ionization energies of meteoric ablation products relative to air species. The low ionization energies of ablation products, such as Mg and Ca, provide strong photoionization and atomic line absorption in regions of the spectrum that air species do not. MgO and CaO are also shown to provide significant absorption. Turbulence is shown to impact the distribution of ablation products through the shock-layer, which results in up to a 100% increase in the radiative heating downstream of the stagnation

point. To create a database of heat transfer coefficients, the developed model was applied to a range of cases. This database considered velocities ranging from 14 to 20 km/s, altitudes ranging from 20 to 50 km, and nose radii ranging from 1 to 100 m. The heat transfer coefficients from these simulations are below 0.045 for the range of cases, for both laminar and turbulent, which is significantly lower than the canonical value of 0.1. When the new heat transfer model is applied to a Tunguska-like 15 Mt entry, the effect of the new model is to lower the height of burst by up to 2 km, depending on assumed entry angle. This, in turn, results in a significantly larger ground damage footprint than when the canonical heating assumption is used.

Keywords: Ablation, Asteroids, Atmospheric Entry, Meteoroids, Meteors, Simulation

---

1. Introduction

A meteor's mass loss rate is an important factor in determining the potential ground damage threat for a given size, entry velocity, entry angle, and composition [1, 2, 3, 4, 5]. The mass loss rate is written as follows:

$$\frac{dM}{dt} = -C_H \frac{S\rho_\infty V_\infty^3}{2Q} \tag{1}$$

where M is the total mass of the meteoroid, C_H is the heat transfer coefficient, S is the cross-sectional area, V_∞ is the free-stream velocity, and Q is the heat of ablation. A significant uncertainty in applying this equation is C_H, which assuming a spherical geometry for the meteoroid, is written as [6]:

$$C_H = \frac{2\int_0^{\pi/2} q_{rad} sin\theta d\theta}{\frac{1}{2}\rho_\infty V_\infty^3} \tag{2}$$

where θ is the angle from the stagnation point, q_{rad} is the radiative heating as a function of θ, and ρ_∞ is the free-stream density. This equation assumes convective heating is negligible relative to radiative heating, which is true for all cases considered in this work that include coupled ablation. A common assumption in asteroid threat assessment studies [2, 5] is to set C_H to 0.1. This constant

value is based on the nonablating, inviscid, stagnation-line analysis by Page et al. [7, 8], which included coupled radiation (meaning the radiative energy source terms are coupled to the flowfield energy equations). Since the work of Page et al. in 1968, significant advancements have been made in modeling the heating environment relevant to meteor entries [9]. Leveraging these advancements, the present work develops chemically reacting Navier-Stokes flowfield simulations that include coupled ablation [10, 11, 12] (meaning the injection of ablation products into the flowfield is modeled), in addition to coupled radiation. While these phenomena have been modeled previously in inviscid stagnation line analyses, the present work represents the first coupled radiation and ablation meteor simulations performed with Navier-Stokes flowfield solvers at altitudes below 50 km, which is the important range for potentially hazardous impacts. In addition to treating viscous effects, the present Navier-Stokes flowfield solver also allows surface regions downstream of the stagnation point to be simulated, which is required to accurately compute an effective C_H for the body. The goals of this work are therefore to assess the impact of coupled radiation and ablation on q_{rad} at meteor entry conditions, to compare the resulting C_H values with the constant 0.1 value, to develop a C_H correlation based on these detailed solutions, and finally to demonstrate the impact of this new model (relative to the constant 0.1 model) for a sample asteroid threat analysis.

This paper is separated into four primary sections: the first considers coupled radiation, the second considers coupled ablation, the third compiles the C_H database, and the fourth applies the developed C_H model to a Tunguska-like entry scenario. The first of these sections, Section 2, begins by presenting details of the coupled radiation flowfield simulation. It then examines the impact of nose radii and altitude on the coupled radiation influence, as well as the impact of the radiative precursor. Similarly, Section 3 begins by presenting details of the coupled ablation flowfield and radiation models. It then examines the impact of coupled ablation on q_{rad} and shows the influence of modeling boundary layer turbulence. Section 4 applies the full coupled radiation and ablation model developed in the previous two sections to create a database of C_H values, which

may be used for meteoroid entry simulations. Finally, Section 5 applies the new C_H model to a Tunguska-like (15 Mt) entry scenario to illustrate its effect on predicted airburst properties.

2. Impact of Coupled Radiation

The potential of meteoroids to reach altitudes below 50 km, while maintaining velocities above 14 km/s, makes the treatment of coupled radiation essential for simulating accurate radiative heating values. Details of the coupled radiation model developed for this analysis are presented in subsection 2.1. Subsection 2.2 then examines the impact of coupled radiation on a meteor flowfield, and identifies unique features that are not seen for more commonly studied reentry vehicles. Finally, subsection 2.3 examines the impact of the free-stream gas, ahead of the meteoroid, absorbing shock layer radiation, also referred to as precursor absorption.

2.1. Flowfield and Radiation Modeling for Coupled Radiation

This work applies NASA's LAURA v5 Navier-Stokes solver [13]. Because altitudes below 50 km are considered here, along with nose radii of 1 m or greater, the impact of thermal nonequilibrium is expected to be small, at least in the forebody region, which is exclusively considered in the current work. Therefore, a single temperature model is used (except for the study of precursor absorption, which required a two-temperature model). Chemical nonequilibrium is treated to allow the present models to be applied in the future to wake simulations, where chemical nonequilibrium effects are significant. For the present cases without ablation, the following 13 species are treated in the flowfield: N, N^+, N^{++}, O, O^+, O^{++}, N_2, N_2^+ O_2, O_2^+, NO, NO^+ and e^-. Thermodynamic properties for N, N^+, N^{++}, O, O^+, and O^{++} are obtained from the high-temperature curve fits developed by Johnston et al. [9]. For the remaining species, the thermodynamic properties are obtained from Gordon and McBride [14]. The transport properties are obtained from Wright et al. [15, 16] where

available. The remaining species are treated using the approximate approach of Svehla [17] modified as suggested by Park [18]. Laminar flow is assumed for all simulations in this section. An axisymmetric hemisphere grid with 128 points in the body-normal direction and 32 points along the surface was applied for all cases.

All radiation computations are made using the HARA radiation code [19]. For air species, HARA applies a comprehensive set of radiation properties, including spectral data and non-Boltzmann models for diatomic molecules and atomic species, which were critically assessed and chosen in studies by Johnston et al. [20, 21]. The accuracy of HARA's predictions for high-temperature air, at conditions relevant to meteor shock layers, has been assessed through comparisons with shock tube measurements [22, 23, 24]. These studies show that measurements and HARA simulations agree within 30% at equilibrium conditions.

Coupled radiation refers to a flowfield computed with the divergence of the radiative flux (S_{rad}) included in the flowfield energy equations [25]. This is in contrast to the uncoupled radiation approach, where the flowfield is computed with S_{rad} set to zero, followed by the radiative heating being computed from this flowfield as a post-processing step. Therefore, in the uncoupled approach the flowfield computation is completely uncoupled from the radiation computation, and fails to account for important phenomena such as radiation absorption in the flowfield, or nonadiabatic cooling of the shock layer. Because of the significant impact of S_{rad} on the flowfield, this uncoupled approach will be shown to be unacceptable for meteor entry conditions.

For coupled radiation, the divergence of the radiative flux is written for a point z in the flowfield as

$$S_{rad,\nu}(z) = 4\pi j_\nu(z) - \kappa_\nu(z) \int_{4\pi} I_\nu d\Psi \tag{3}$$

where the first term represents the emitted energy and the second term represents the energy absorbed from the incoming radiation from the surrounding flowfield. A recent study by Johnston and Mazaheri [26] showed that the sec-

ond term in this equation may be accurately approximated by the tangent-slab approximation, which reduces the computational cost of evaluating this term by two orders of magnitude. The tangent-slab approximation, which is applied in this work, assumes one-dimensional radiative transport along body-normal rays through the shock layer. This approximation allows S_{rad} to be written as

$$S_{rad,\nu}(z) = \frac{d(q^{+}_{rad,\nu} - q^{-}_{rad,\nu})}{dz} \tag{4}$$

where $q^{+}_{rad,\nu}$ and $q^{-}_{rad,\nu}$ are the shock- and wall-directed radiative flux, respectively. Note that the value of $q^{-}_{rad,\nu}$ at z=0 is the radiative heating to the surface of the meteoroid.

To avoid numerical instabilities, S_{rad} is typically set to zero in the free-stream. This approach will be applied for the coupled radiation simulations presented in this work, except for the study of precursor absorption in Section 2.3. To model precursor absorption, the radiation computation is extended into the free-stream. Furthermore, photochemical source terms computed in HARA, resulting from photoionization and photodissociation, are coupled to the flowfield species continuity equations. Additional details regarding the photochemical source terms and precursor absorption, along with their impact on the radiative heating, are presented in Section 2.3.

The typical impact of including this S_{rad} term is the reduction of the shock layer temperatures relative to the uncoupled values, which is the result of radiative emission reducing the total enthalpy of the shock layer [27]. Because meteoroids tend to reach lower altitudes at higher velocities than reentry vehicles, and because of the larger potential size of a meteoroid, the optical thickness of a meteoroid shock layer can be significantly larger than for a reentry vehicle. This larger optical thickness results in a fundamentally different S_{rad} distribution through the shock layer, which changes the resulting coupled radiation temperature distribution [28]. Examples of this behavior are presented in the following paragraphs.

2.2. Impact of Coupled Radiation on Stagnation Line

Figure 1(a) compares the uncoupled and coupled stagnation line temperatures for a case with a velocity of 20 km/s and altitude of 30 km. Results for both a radius of 10 m and 30 m are presented. The impact of coupled radiation is seen to reduce the temperatures through the layer similarly for both nose radii. These decreased temperatures are the result of radiative energy being emitted out of the shock layer, therefore decreasing the total enthalpy of the flow. Because the shock layer pressures remain essentially constant between the coupled and uncoupled solutions, the shock layer density must increase to accommodate the decreased temperatures for the coupled radiation case. Through mass conservation, this increased density leads to the large decrease in shock standoff distance seen in Fig. 1(a) for the coupled radiation cases. Furthermore, coupled radiation is seen to increase the boundary layer thickness dramatically for both nose radii. Note that these thicker boundary layers are due purely to coupled radiation (in particular, the shape of the S_{rad} profile), and not viscosity. These coupled radiation boundary layers will be discussed further in the following paragraphs. Figure 1(b) shows that because this boundary layer is thicker for the 30 m case, it is able to provide more absorption for q^-_{rad}. The resulting q^-_{rad} values at the wall are 38 and 28 W/m^2 for the 10 and 30 m cases, respectively. Although not clearly seen in Fig. 1(b), the coupling ratio (coupled/uncoupled radiative heating) is 0.20 and 0.16 for the 10 and 30 m cases, respectively. This lower coupling ratio for the larger radius case indicates that the impact of coupled radiation increases slightly with increasing nose radius.

In addition to the impact of varying nose radius on coupled radiation, varying the free-stream density or altitude has a significant impact on the coupled radiation behavior. For altitudes above 40 km, the shock layer is not optically-thick at 20 km/s, meaning S_{rad} is nonzero across the layer and q^-_{rad} is below the Planck function (q_{Planck}). This behavior is similar to that seen for reentry vehicles. Figure 2 presents an example of this regime, which consists of a 10 m radius case at 20 km/s and an altitude of 50 km. Figure 2(a) confirms the nonzero S_{rad} values through the middle of the layer for the uncoupled case.

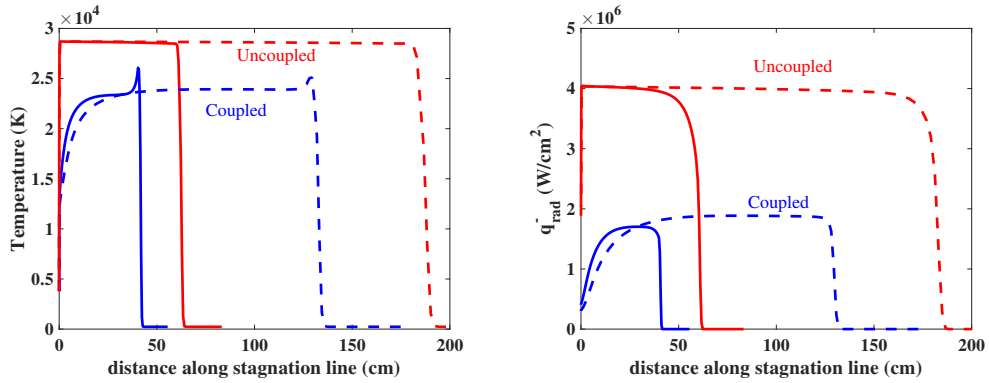

(a) Temperature

(b) Wall-directed radiative flux

Figure 1: Impact of increasing nose radius (R_N) on coupled radiation impact (Solid lines: R_N=10 m, Dashed lines: R_N=30 m).

These nonzero values lead to the continuous decrease in temperatures, moving from the shock to the wall, shown in Fig. 2(b) for the coupled case. Figure 2(c) shows that these decreased temperatures for the coupled case result in an 80% reduction in q_{rad}^{-} reaching the surface. This figure also confirms that q_{rad}^{-} is well below q_{Planck} throughout the inviscid region of the flow for both the coupled and uncoupled cases, which is consistent with the nonzero S_{rad} values. Close to the surface, however, q_{rad}^{-} becomes larger than q_{Planck}, which is the result of the sharply decreasing temperature gradient.

For altitudes below 40 km, the shock layer becomes optically thick at 20 km/s, meaning S_{rad} approaches zero near the middle of the layer and q_{rad}^{-} reaches q_{Planck}. Figure 3 presents an example of this regime, for a 10 m radius case at 20 km/s and an altitude of 30 km. Note that this case is the same as that in the previous paragraph, except the altitude has been lowered from 50 to 30 km. Figure 3(a) confirms that S_{rad} approaches zero throughout the middle of the shock layer for the uncoupled case. As shown in Figure 3(b), the nonzero S_{rad} values concentrated near the shock and wall lead to temperature gradients near the shock and wall for the coupled case. Note that coupled temperature profiles may be loosely inferred from the uncoupled S_{rad} profiles by recognizing

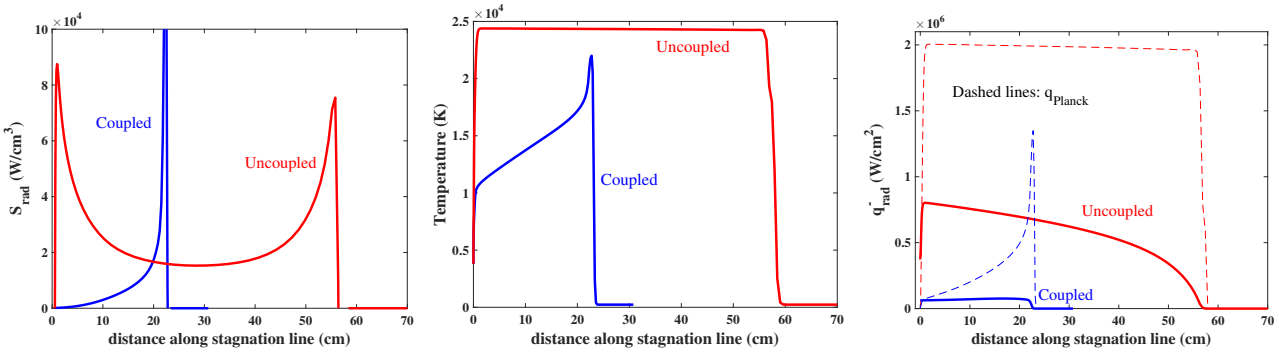

(a) (b) (c)

Figure 2: Impact of coupled radiation for the 50 km altitude case (with a velocity of 20 km/s and nose radius of 10 m).

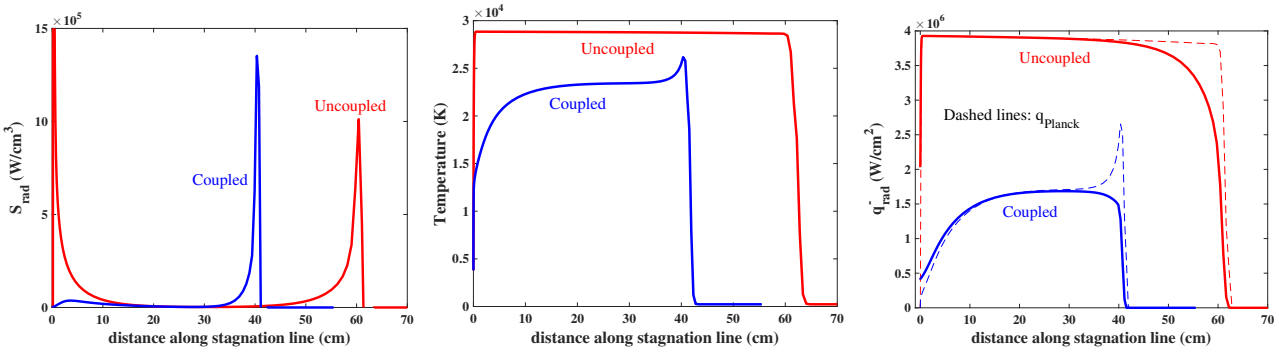

(a) (b) (c)

Figure 3: Impact of coupled radiation for the 30 km altitude case (with a velocity of 20 km/s and nose radius of 10 m).

that positive S_{rad} values lead to a decreasing coupled temperature gradient (moving from the shock to the wall). The temperatures through the center of the layer are nearly constant due to the local S_{rad} values near zero. This regime of coupled radiation, where the temperature gradients are limited to narrow regions near the shock and wall, is not seen in the study of reentry vehicles. Recall that although these temperature gradients appear to be the result of a thick viscous boundary layer and post-shock nonequilibrium region, they are actually due to the radiation coupling and, specifically, to the fact that S_{rad} approaches zero in the middle of the shock layer. Although this behavior has been discussed in previous studies by Goulard [28] and Biberman [29], it has not previously been studied with modern shock-capturing flowfield codes.

To summarize the present discussion regarding the impact of nose radius and altitude on the impact of coupled radiation, Fig. 4(a) presents the ratio of coupled to uncoupled radiative flux for a range of nose radii and altitudes, all with a velocity of 20 km/s. This figure confirms that the impact of coupled radiation increases with increasing nose radius for all cases, regardless of the optical thickness. The increasing impact of coupling with increasing altitude is the result of the decreased optical thickness at higher altitude, which allows for the nonzero S_{rad} values across the layer. This trend can also be seen by comparing Figs. 2 and 3.

Figure 4(b) presents the stagnation-point radiative heating values for the 20 km/s cases. This figure shows that, for the non-optically-thick conditions at 50 km, increasing the nose radius increases the radiative heating. Conversely, for the optically-thick cases at 20 and 30 km altitudes, the radiative heating decreases with increasing nose radius. Recall that this decrease with increasing radius is due to the larger coupled wall layer shown in Fig. 1. The increased radiative heating with increasing radius is the typical trend seen for non-optically-thick reentry vehicles, where the larger shock standoff distance provides a larger path length of radiating gas.

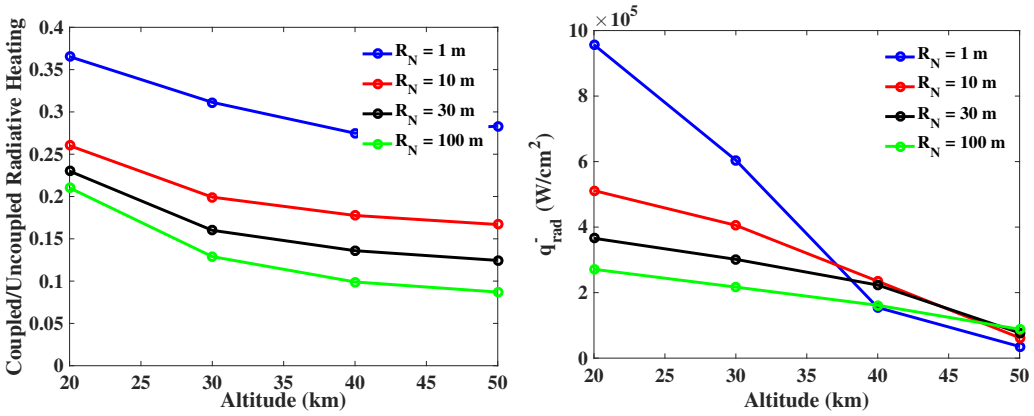

(a) Coupled/Uncoupled heating ratio.

(b) Radiative heating with coupled radiation.

Figure 4: Stagnation point coupled radiation values at 20 km/s.

2.3. Impact of Precursor Absorption

The preceding coupled radiation analysis assumed the radiative flux leaving the shock layer was not absorbed in the free-stream gas, thereby ignoring any precursor absorption impact. This assumption was enforced by setting S_{rad} to zero ahead of the shock, which was detected when temperatures fell below 2000 K. This assumption is typically applied for coupled radiation simulations for four primary reasons. First, to sufficiently model the precursor, the computational grid must extend far into the free-stream (at least the distance of 10 shock layer thicknesses). This slows down both the flowfield and radiation solutions. Second, radiation and two-temperature flowfield modeling of the low-temperature free-stream gas contains significant uncertainty. Third, photochemical processes, such as photodissociation and photoionization, have a significant impact on the flowfield species continuity equations in the precursor. This increased importance of photochemical source terms in the precursor is due to collisional processes being weakened by the low free-stream number densities. Computing the photochemical source terms requires additional solutions of the radiative transport equations, which slows down the simulation. Fourth,

a two-temperature model is required in the precursor, even if the shock layer is in strong thermochemical equilibrium, which further slows down convergence.

Johnston et al. [30] considered the precursor impact for a 5 m radius sphere at 15 km/s and an altitude of 60 km. This study found a radiative heating increase of 20% due to treating the precursor. A similar increase of 15% was reported later by Johnston et al. [9] for a 1 m radius sphere at 22 km/s and an altitude of 60 km. The model applied for these studies is presented in Johnston et al. [19], which contains the photochemical processes listed in Table 1. Not only do these processes provide the dominant absorption for the free-stream gas, which impact the precursor temperatures through S_{rad}, but they also noticeably impact the species continuity equations as a photochemical source term. In addition to applying the processes listed in Table 1, the precursor model also requires a correction to S_{rad} to account for the non-tangent-slab geometry of the precursor as the distance from the shock layer increases. This correction, which was developed by Stanley and Carlson [31], is applied as follows:

$$S_{rad,\nu} = \frac{dq^{-}_{rad,\nu}}{dz} + \phi_{\nu}\frac{dq^{+}_{rad,\nu}}{dz} \tag{5}$$

Following Stanley and Carlson [31], the correction factor ϕ_ν is written as

$$\phi_{\nu} = 1 - cos^2\beta\frac{0.5 - E_3(\tau_{\nu}sec(\beta))}{0.5 - E_3(\tau_{\nu})} \tag{6}$$

where E_3 is the third exponential integral, and τ_ν is the optical depth computed from the wall to the point in the precursor. The angle β is one-half of the angle subtended by the body, computed as

$$\beta = sin^{-1}\frac{R_N + z_s}{R_N + z} \tag{7}$$

where R_N is the nose radius of the meteoroid, z_s is the shock standoff, and z is the distance along the body normal. Equations 6 and 7 are applied for points in the precursor, defined as all points where $z > z_s$. Note that at $z = z_s$ the correction termed ϕ_ν is equal to one, while as z becomes large ϕ_ν goes to zero. Johnston and Mazaheri [26] confirmed the accuracy of this approach through the application of a detailed ray-tracing approach.

Table 1: Photochemical processes applied in the present study.

#	Process		Spectral Range	Data Source
1	N_2 Photodissociation:	$N_2 + h\nu \leftrightarrow 2N$	9.8 eV $< h\nu$	Stanley and Carlson[31]
2	O_2 Photodissociation:	$O_2 + h\nu \leftrightarrow 2O$	7.1 eV $< h\nu$	Mnatsakanyan[32]
3	N_2 Photoionization:	$N_2 + h\nu \leftrightarrow N_2^+ + e^-$	12.4 eV $< h\nu$	Romanov et al.[33]
4	O_2 Photoionization:	$O_2 + h\nu \leftrightarrow O_2^+ + e^-$	9.7 eV $< h\nu$	Romanov et al.[33]
5	N Photoionization:	$N + h\nu \leftrightarrow N^+ + e^-$	12.4 eV $< h\nu$	TOPbase [34]
6	O Photoionization:	$O + h\nu \leftrightarrow O^+ + e^-$	9.7 eV $< h\nu$	TOPbase [34]

To assess the impact of the precursor absorption for conditions relevant to meteors, the precursor model discussed in the previous paragraph was applied to the previously considered 30 and 50 km altitude cases (with a radius of 10 m and velocity of 20 km/s). Figure 5 presents stagnation line properties for the 30 km case. Figures 5(a) and 5(b) show the temperatures and mass fractions, respectively, along the entire computational range of the stagnation line, which extends 5 m from the nose. The bow shock is located near 45 cm, where the temperature spikes above 25,000 K. Starting from the outer boundary at 500 cm and moving toward the shock, the vibrational-electronic temperature rises gradually due to absorption until 100 cm. A negligible change in the mass fractions is seen up to this point. Immediately below 100 cm, O_2 dissociates completely and N_2 begins to dissociate, while the vibrational-electronic temperature rises rapidly to a peak at 75 cm. Below this point, ionization of O becomes significant and provides enough electrons to begin equilibrating the two temperatures through electronic-translational energy relaxation [35]. This thermal equilibration reduces the vibrational-electronic temperature and increases the translational-rotational temperature until the shock is reached at 45 cm, at which point both temperatures increase. Figures 5(c) and 5(d) compare the temperatures with and without precursor modeling for the first 100 cm away from the surface. For the precursor case, the enthalpy crossing the shock is increased by the free-stream absorption, which results in the higher shock layer temperatures in the outer region of the shock layer. However, because of the optical thickness of the shock layer, where radiation emitted below 10 cm and

toward the shock is completely absorbed before it reaches the shock, this region below 10 cm is not influenced strongly by the including the precursor (i.e., S_{rad} in this region is not influenced). This weak precursor influence near the wall results in a negligible change to the temperatures below 10 cm with the addition of the precursor. Although the q_{rad}^{-} values above 10 cm are higher for the precursor case, the similar temperature profiles below 10 cm result in q_{rad}^{-} reaching the surface to be within 2%. Note that the precursor may have a significantly larger impact on the radiative flux emitted from the shock layer to a distant observer. This "observed" radiative flux, which will also likely be influenced significantly by the wake, will be the subject of a future study.

For the 50 km case, Fig. 6 presents the same set of figures as shown for the 30 km case. The temperature profiles presented in Fig. 6(a) show that the vibrational-electronic temperatures remain above 5000 K until a distance of 200 cm, while for the 30 km case this distance was only 100 cm. This larger precursor region for the 50 km case is the result of its lower free-stream density, which is 1% of the 30 km value. This lower free-stream density decreases the optical thickness, which increases the length of free-stream gas required to absorb the radiation emitted from the shock layer. The precursor impact on the first 100 cm of the shock layer for this 50 km case is shown in Fig. 6(c) and Fig. 6(d). Strong absorption near 26 cm leads to a sharp increase in temperature, which provides an increase in q_{rad}^{-}. At the surface, including the precursor results in a 25% increase in q_{rad}^{-}. Although the temperatures near the wall are similar for the precursor and no-precursor cases, the 50 km case is not as optically-thick as the 30 km case. This acts to reduce the impact of the temperatures near the wall on the radiative heating. The 25% increase in the radiative heating seen here may be considered an upper-limit for the precursor influence. Simulations presented in the remainder of this paper do not include the precursor. Note that the significant absorption due to ablation products shown in the next section would likely diminish this 25% precursor influence. This is expected because ablation products will be shown to significantly increase the optical thickness of the boundary layer.

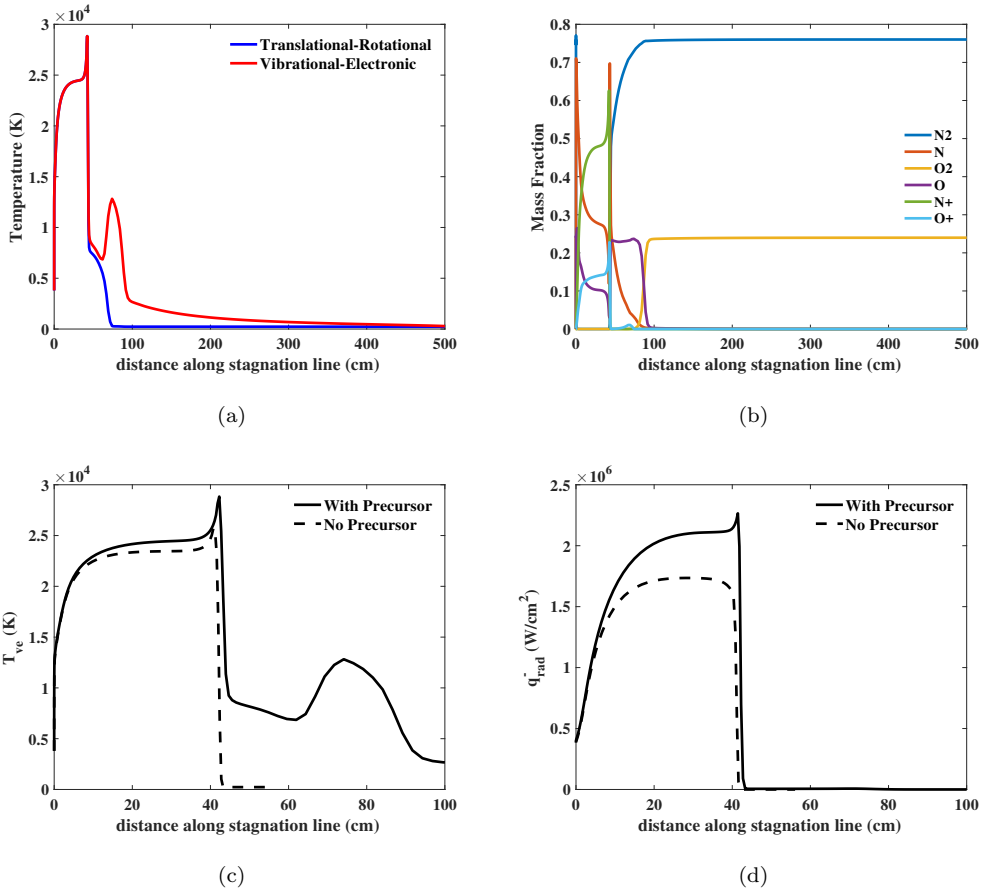

Figure 5: Precursor simulations for the 30 km altitude case.

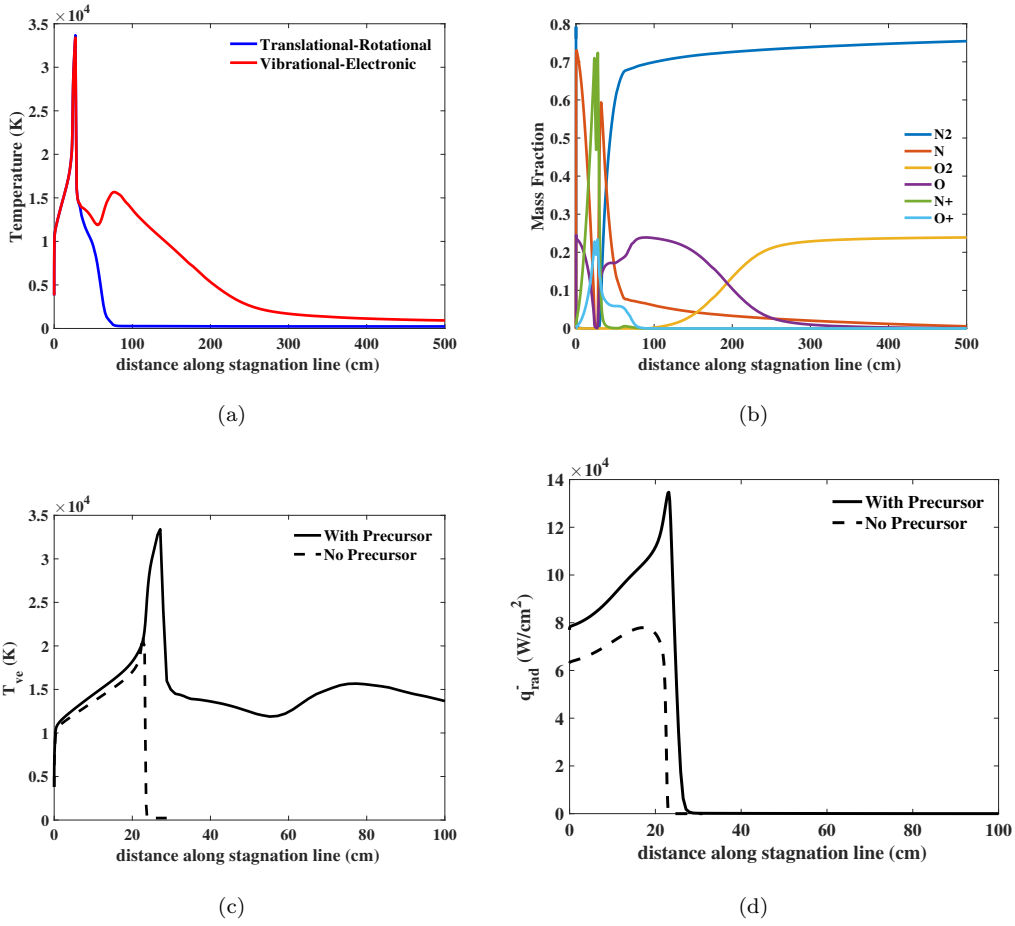

Figure 6: Precursor simulations for the 50 km altitude case.

3. Impact of Coupled Ablation

This section examines the impact of coupled ablation on the radiative heating. Coupled ablation is defined as the modeling of an ablating surface boundary condition within the flowfield computation. As will be shown, this coupled ablation approach is essential for modeling the aerothermodynamic environment of meteors because of their relatively large ablation rates, which significantly alter the structure of the flow near the surface. Furthermore, coupled ablation introduces species into the flow that greatly alter the radiative environment. The present section investigates this coupled ablation impact by first developing a coupled ablation model appropriate for meteors, which is presented in subsection 3.1. This is followed by the detailed study of two cases in subsection 3.2, which provides insight into the influence of coupled ablation on the flowfield structure and radiative heating. Finally, the impact of boundary layer turbulence on the coupled ablation environment is investigated in subsection 3.3.

3.1. Flowfield and Radiation Modeling for Coupled Ablation

The ablating surface boundary condition for this analysis is simplified by the massive ablation present for meteor entries at the conditions of present interest (velocities greater than 14 km/s at altitudes below 50 km). The presence of massive ablation, where the boundary layer is blown off the surface, results in elemental mass fractions at the surface equal to those of the surface material. This is in contrast to weaker ablation cases, such as the diffusion-limited oxidation regime, where the elemental mass fractions at the surface are a combination of the surface material and boundary layer edge gas. With the assumption that the elemental mass fractions at the surface are equal to those of the surface material, the surface temperature (T_w) and enthalpy (h_{abl}) may be curve-fit as a function of surface pressure (p_w) as follows:

$$T_w = 3021.0 - 209.59ln(p_w) + 40.097ln(p_w)^2 - 2.1897ln(p_w)^3 + 0.057422ln(p_w)^4 \tag{8}$$

$$h_{abl} = 1.1235\times10^{7} - 1.7419\times10^{6} ln(p_w) + 2.2495\times10^{5} ln(p_w)^2 - 1.2814\times10^{4} ln(p_w)^3 + 2.7686\times10^{2} ln(p_w)^4 \quad (9)$$

where p_w has units of Pa, T_w is in K, and h_{abl} is in J/kg. The data for these curve-fits were provided by Chen [36] for an LL-Chondrite meteoroid. For the surface pressures of interest, h_{abl} has a value of nearly 6.2 MJ/kg. Combining h_{abl} with the heat of fusion, which is approximately 2 MJ/kg, results in a value near the empirically derived 8.26 MJ/kg [37] that is typically applied for Q in Eq. (1). For the present study, h_{abl} considers only ablation due to vaporization, which ignores melting and the heat of fusion. This is a good approximation for the stagnation region of meteoroids with nose radii greater than 1 m, where the melt layer is thin and removed rapidly from the surface (this removal would have a minimal impact on the flowfield because it does not introduce gaseous species). However, for shoulder regions or for smaller meteoroids, removal of melt could have a significant impact on the surface energy balance. This impact is beyond the scope of the present work.

The ablation rate $\dot{m}$ is computed from these curve-fits and the surface energy balance:

$$\dot{m} = \frac{q_{rad}\alpha + q_{conv} - \epsilon\sigma T_w^4}{h_{abl}} \quad (10)$$

where α is the absorptivity and ϵ is the emissivity of the surface, which are both set to unity for this work. Recall that for the present cases, q_{conv} is negligible and $\epsilon\sigma T_w^4$ is less than 15% of q_{rad}. For this equation to be consistent with Eq. (1), C_H should include these additional terms. The C_H values presented later in this work apply Eq. 2, which only includes q_{rad}. The surface species are computed assuming chemical equilibrium at the surface pressure, temperature, and elemental composition.

The elemental mass fractions of the surface material, which represent an LL-Chondrite meteoroid, were assumed as follows [36]: O = 0.457, Si = 0.206, Fe = 0.172, Mg = 0.120, Na = 0.005, S = 0.020, Al = 0.010, Ca = 0.010. To account for the addition of these elements to the 13 species air chemistry,

the following 26 species were added to the LAURA flowfield simulations: Fe, Fe^+, FeO, Mg, Mg^+, MgO, Si, Si^+, SiO, SiO_2, Fe^{++}, Mg^{++}, Si^{++}, S, S^+ SO, SO_2, Al, Al^+, AlO, Ca, Ca^+, CaO, Na, Na^+, and NaO. The thermodynamic properties for atomic neutrals and ions were computed using electronic levels from NIST, which were also implemented in the HARA radiation computation, to ensure that Saha-Boltzmann and Boltzmann electronic state populations are coincident. This behavior is required to accurately apply nonequilibrium radiation models for these species. Although the current forebody simulations are strongly equilibrated, therefore making negligible the influence of nonequilibrium radiation, future work that will utilize these simulations will include a wake and radiative signature computation, which are strongly influenced by nonequilibrium. Besides atomic neutrals and ions, the thermodynamic properties for the remaining species are taken from Gordon and McBride [38]. The flowfield rate model for these species is presented in Table 2. Again, the influence of these rates will primarily be seen in future work, as the present strongly equilibrated forebody simulations are insensitive. Note that the electron-impact ionization rates are based on the rate for atomic nitrogen, which is scaled using the ionization energy. This approach is taken by Park [39] to obtain the electron-impact ionization rates commonly applied for C and O.

Solutions of Eqs. (8) - (10) were obtained every 50,000 flowfield solution iterations, and a relaxation factor of 0.3 was applied to the ablation rate. This relaxation factor is required because changing the ablation rate influences the species profiles and temperatures, which impact the radiative heating and S_{rad} distributions.

Except for cases where the precursor is treated in Section 2.3, photochemical source terms are not included in the flowfield, because of their added computational expense. For air shock layers, this assumption is common for altitudes below 70 km, where shock layer number densities are relatively high, except in the free-stream or wake. Photochemical source terms have a negligible impact in regions of large number densities because collisional rates scale with number density squared, while photoionization and photodissociation scale linearly with

Table 2: Chemical kinetics for meteor ablation products.

i	Reaction	$A_{f,i}$	$n_{f,i}$	$D_{f,i}$	Ref.
1	$Si + e^- \leftrightarrow Si^+ + e^- + e^-$	2.5e+34	-3.82	9.46e+4	Based on N rate [18]
2	$Fe + e^- \leftrightarrow Fe^+ + e^- + e^-$	2.5e+34	-3.82	9.17e+4	Based on N rate [18]
3	$Mg + e^- \leftrightarrow Mg^+ + e^- + e^-$	2.5e+34	-3.82	8.87e+4	Based on N rate [18]
4	$Si + NO \leftrightarrow SiO + N$	3.2e+13	0.0	1775.0	Mick et al. [40]
5	$Si + O_2 \leftrightarrow SiO + O$	2.1e+15	-0.53	16.83	Le Picard et al. [41]
6	$SiO + M \leftrightarrow Si + O + M$	4.0e+14	0.0	9.56e+4	Estimate
7	$SiO_2 + M \leftrightarrow SiO + O + M$	4.0e+14	0.0	9.56e+4	Estimate
8	$Fe + O_2 \leftrightarrow FeO + O$	1.3e+14	0.0	1.02e+4	Akhmadov et al. [42]
9	$Mg + O_2 \leftrightarrow MgO + O$	5.1e+10	0.0	0.0	Hodgson and Mackie [43]
10	$SO + O \leftrightarrow S + O_2$	2.4e+07	1.51	2.53e+3	Lu et al. [44]
11	$SO_2 + S \leftrightarrow SO + SO$	4.8e+14	0.0	1.08e+4	Murakami [45]
12	$O_2 + SO \leftrightarrow SO_2 + O$	2.3e+12	0.0	3.70e+3	Garland [46]
13	$Al + O_2 \leftrightarrow AlO + O$	2.0e+13	0.0	0.0	Cohen and Westberg [47]
14	$Al + SO_2 \leftrightarrow SO + AlO$	9.6e+13	0.0	2.00e+3	Fontijn and Felder [48]
15	$Al + e\text{-} \leftrightarrow Al^+ + e\text{-} + e\text{-}$	2.5e+19	-0.82	6.94e+4	Based on N rate [18]
16	$NaO + O \leftrightarrow Na + O_2$	2.2e+14	0.0	0.0	Plane and Husain [49]
17	$Na + e\text{-} \leftrightarrow Na^+ + e\text{-} + e\text{-}$	2.5e+19	-0.82	5.96e+4	Based on N rate [18]
18	$Ca + O_2 \leftrightarrow CaO + O$	2.5e+14	0	7.25e+3	Kashireninov et al. [50]
17	$Ca + e\text{-} \leftrightarrow Ca^+ + e\text{-} + e\text{-}$	2.5e+19	-0.82	7.09e+4	Based on N rate [18]

number density. Because the present cases are all at 50 km or lower in altitude, this assumption is expected to remain valid for air species. However, with the introduction of ablation products with low ionization potentials, such as Mg and Ca, this assumption requires a reevaluation. Simulations at 30 and 50 km altitudes were performed with the photoionization source terms from all atomic ablation products. Comparing these cases with those lacking the photoionization source terms, the resulting radiative heating values are within 1% for the 30 km case and 2% for the 50 km case. These differences are for the shoulder, or maximum radius location of the sphere, where the disagreement is largest. At the stagnation point, the values are within 0.5%. This good agreement indicates that treating the photochemical source terms is not required for forebody simulations at altitudes below 50 km. Therefore, these terms were not included in the other simulations reported in this paper.

Table 3: Summary of molecular band modeling for meteor ablation products.

Specie	Transition	Spectral Range (eV)	Data Source
SiO	A-X	4.54-5.79	Franck-Condon factors and energy levels from Geier et al. [53], and band oscillator strength from Park and Arnold [54].
SiO	E-X	5.74-7.55	Franck-Condon factors and band oscillator strength taken from Naidu et al. [55] and Drira [56], and energy levels from Lagerqvist [57].
FeO	Orange	1.68-2.38	Oscillator strengths and energy levels taken from Michels [58].
MgO	B-A	1.72-2.45	Oscillator strengths and energy levels taken from Daily [59] and Bell et al. [60].
MgO	D-A	1.72-2.45	Oscillator strengths and energy levels taken from Naulin et al. [61] and Bell et al. [60].
MgO	B-X	2.38-2.69	Oscillator strengths and energy levels taken from Daily [59] and Bell et al. [60].
CaO	A-X	1.1-2.0	Oscillator strengths and energy levels taken from Doherty [62] and Liszt [63].
CaO	B-X	2.6-3.7	Oscillator strengths and energy levels taken from Pasternack [64] and Liszt [63].
CaO	Orange	1.7-2.2	Oscillator strengths and energy levels taken from Pasternack [64] and Liszt [63].
CaO	Green	1.7-2.2	Oscillator strengths and energy levels taken from Pasternack [64], Liszt [63], and Baldwin [65].
SO	A-X	3.8-5.0	Franck-Condon factors and band oscillator strength taken from Borin [66] and energy levels from Rosen [67].
AlO	B-X	2.2-3.0	Oscillator strengths and energy levels taken from Borovicka [68].

Many of the 26 additional species added to the flowfield to account for meteor ablation products have a significant impact on the shock layer radiation. To account for this impact, radiation models were developed and added to the HARA code. For each neutral atomic species, an atomic line model was developed based on energy levels and line strengths from NIST. For each line, Stark broadening widths were obtained from Griem [51], where available, and a correlation [20] otherwise. Atomic line models for ionized species were also developed, but were found to have a negligible influence. Atomic photoionization cross sections for atomic neutrals and ions were obtained from TOPbase [34]. As with atomic lines, only the photoionization from atomic neutrals provide a noticeable impact on the radiative heating. For molecular band systems, Table 3 summarizes the band systems treated and the source of modeling data used for each. Many of these band system models are based on the work of Park [52].

3.2. Impact of Coupled Ablation on the Stagnation Line at 20 km/s

To provide insight into the impact of coupled ablation on the shock layer environment, cases at 30 and 50 km altitude are studied, both with a velocity of 20 km/s and a radius of 10 m. These are the same two cases which were presented in Section 2 to investigate the impact of coupled radiation. Note that all coupled-ablation results presented here also include coupled radiation. For the high-pressure 30 km case, Fig. 7 presents the stagnation-line temperatures, ablation product mole fractions, and wall-directed radiative flux (q^-_{rad}). For the temperature and q^-_{rad} profiles, comparisons are made between the coupled ablation and no-ablation cases (this no-ablation case corresponds to the coupled radiation result from the previous section). Considering the temperature profiles in Fig. 7(a), coupled ablation is seen to increase the shock standoff distance. This increased shock standoff distance is due to the mass injection at the surface resulting from ablation, which at the stagnation point is 5.1% of the free-stream mass flux for this case. The size of the ablation layer is apparent from the ablation species mole fractions in Fig. 7(b), which extend roughly 6 cm away from the surface. Figure 7(c) shows that, other than the increase in shock standoff distance, the q^-_{rad} profile is similar for the coupled ablation and no-ablation cases, except for near the wall. To clarify this near-wall region, Figs. 7(d) - (f) present the first 4 cm away from the wall for the same profiles shown in (a) - (c). These figures of the near-wall region show that below 1 cm the temperatures for the coupled ablation case are lower than for the no-ablation case. This region corresponds to a rise in the molecular species SiO, MgO, FeO, and CaO, which are restricted to this near wall region. The impact of these ablation species on q^-_{rad} is seen in Fig. 7(f), where below 2.5 cm q^-_{rad} decreases significantly faster for the coupled ablation case, indicating stronger absorption. This absorption is seen to increase as the wall is approached, which corresponds to an increase in the neutral atomic and molecular mole fractions. The resulting value of q^-_{rad} at the wall is more than an order of magnitude lower for the coupled ablation case (1.3 W/m^2) than for the no ablation case (38 W/m^2).

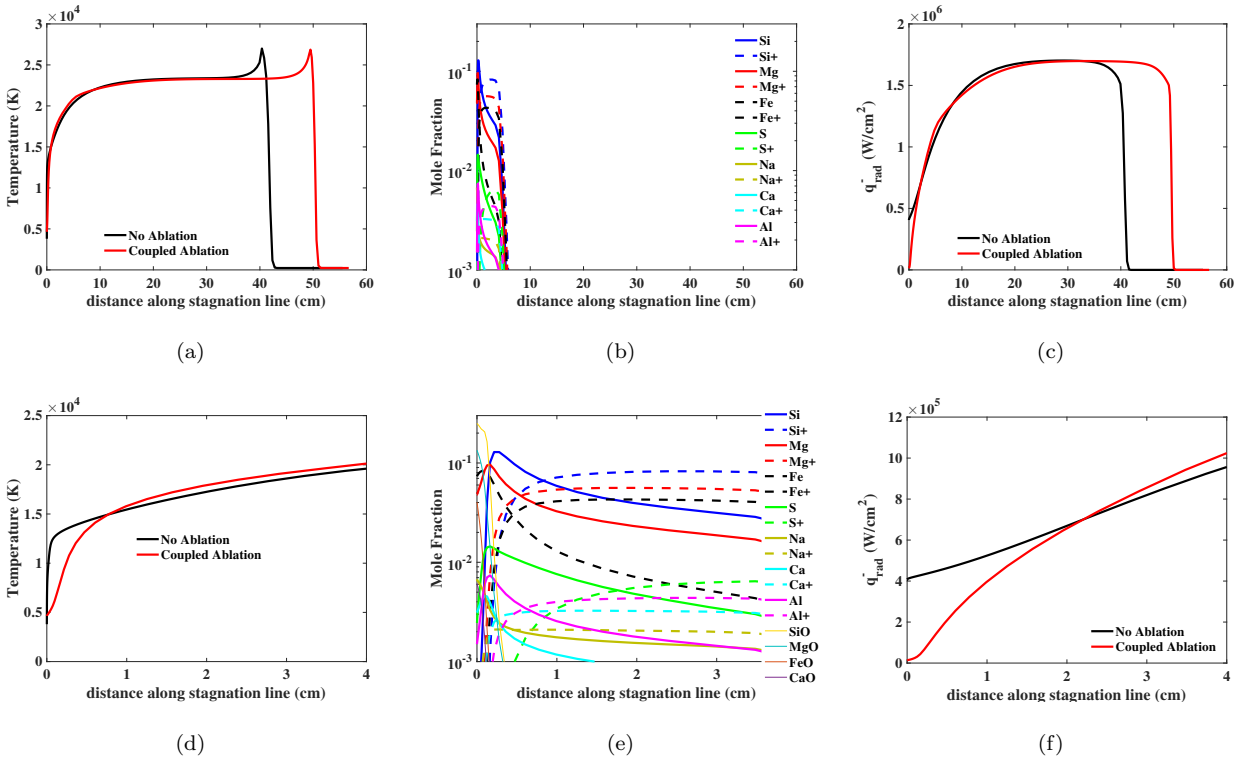

Figure 7: Impact of coupled ablation for the 30 km altitude case.

To further investigate the significant decease in the radiative flux reaching the wall due to coupled ablation, Fig. 8(a) presents the q_{rad}^{-} spectra at four points through the ablation layer. The Planck function is presented for each point as a dashed line. To help interpret each of these spectra, Fig. 8(b) presents the associated absorption coefficient for each case. For distances from the wall (z) above 0.47 cm, the q_{rad}^{-} spectrum follows the Planck function at the local flowfield temperature. This is the result of the absorption coefficients values above 10 cm^{-1} across the entire spectrum shown in Fig. 8(b) combined with minor gradients in temperatures and number densities shown in Fig. 7(d) and 7(e). The minor deviations of the q_{rad}^{-} spectrum from the Planck function for the 0.47 cm case is the result of these gradients. Moving towards the surface to the 0.21 cm point, the deviation from the Planck function increases between 1 and 3 eV. This is due to the increased temperature and number density gradients and decreased absorption coefficients in this spectral range. Moving to the 0.13 cm point, the absorption coefficient below 2 eV is seen to decrease by an order-of-magnitude, which causes a significant deviation between q_{rad}^{-} and the Planck function. Finally, moving to the wall, the q_{rad}^{-} values below 2 eV are reduced only slightly from the values at 0.13 cm, which is due to absorption coefficient values below 2 cm^{-1} over this 0.13 cm thick layer. Above 2 eV, however, the absorption coefficient values greater than 10 cm^{-1} drive most of the q_{rad}^{-} spectrum down to the Planck function at the wall temperature.

Because of the sensitivity of the q_{rad}^{-} spectrum on the absorption coefficient spectrum near the wall, it is insightful to separate the absorption coefficient spectrum into its components. This breakdown is presented in Fig. 9 for the 0.47, 0.13, and 0.0 cm points. For each point, the figure on the left presents the contribution from molecular band systems, the middle figure presents the contribution from atomic photoionization, and the figure on the right presents the atomic line contribution. The vertical scales for each of these figures were fixed to those of Fig. 8(b). When combined with the free-free and induced emission contribution, the values in these figures sum to the values presented in Fig. 8(b). These figures show the anticipated result that moving from the higher temper-

ature point at 0.47 cm towards the wall, the atomic line and photoionization contribution decreases and the molecular band contribution increases. Note also that the atomic lines become significantly narrower as the wall is approached due to decreasing electron number densities (which reduce Stark broadening) and decreasing temperatures (which reduce Doppler broadening).

Considering the 0.47 cm point, the Mg atomic line contribution below 2 eV is dominant, while above 2 eV the Fe lines provide a similar contribution. The photoionization component at this point is also dominated by Mg, but is lower than the line contribution over most of the spectrum shown here. Because of the low molecular number densities at 0.47 cm, the molecular band absorption coefficients are mostly below the lower limit of the vertical scale, except for a few narrow spikes from MgO and SiO bands. Moving to the 0.13 cm point, the narrower atomic lines remain dominant. The lower temperature at this point decreases the atomic line and photoionization contributions below 2 eV, due to lower populations of the upper electronic levels associated with these transitions. This temperature decrease allows the rising MgO and CaO band systems to provide a noticeable contribution below 2 eV. Finally, at the lower temperature wall, the molecular band contributions increase significantly, due to the increased molecular number densities, while the atomic contributions decrease significantly below 3 eV. Note that the lack of any band system to fill the spectrum below 1 eV causes the sharp drop off in the absorption coefficient at the wall shown in Fig. 8(b). If the ablation product elements considered here were replaced with air elements of N and O, these gaps in the absorption coefficient would cover a significant fraction of the spectrum, due to the negligible atomic line and photoionization contribution for air below 8,000 K. This negligible contribution is the result of the significantly higher ionization energies for N and O, which are 14.53 and 13.62 eV, respectively, compared to the meteor ablation products, which are as low as 5.14 and 6.11 eV for Na and Ca, respectively. This observation is the fundamental reason for the dramatic decrease in the radiative heating for coupled ablation cases relative to the no ablation cases.

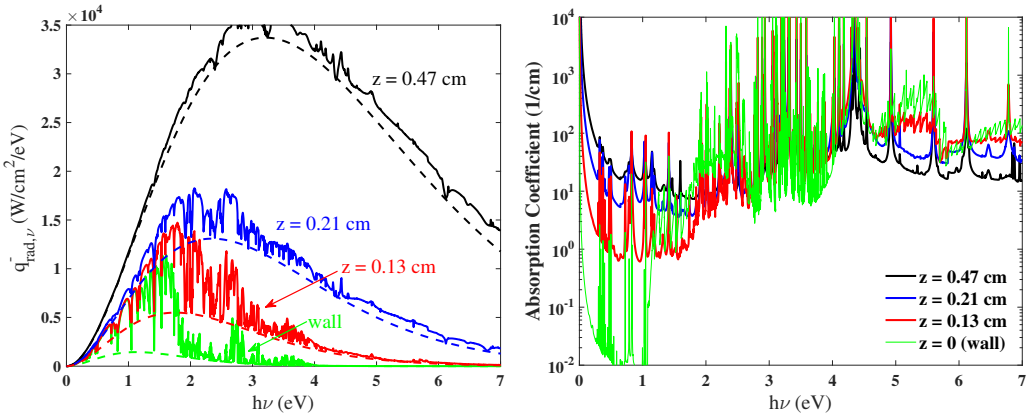

(a) (b)

Figure 8: Spectral details at various points along the stagnation line for the 30 km altitude case.

To further clarify the impact of each ablation product species and radiative process on the radiative heating, Table 4 lists the percent increase in the radiative heating (q^-_{rad} at the wall) due to setting the absorption and emission coefficient spectrum for individual processes equal to zero (this is done as a post-processing step to a converged coupled radiation and ablation flowfield). Processes that have less than a 0.2% impact are not listed. For the present 30 km altitude case (the 50 km case will be discussed later), the dominant atomic processes are provided by Mg, as anticipated from Fig. 9. Although Fe lines appear to be stronger than Ca lines in this figure, the location of the Fe lines coincide closely with Mg, while the peak Ca lines are located near 2 eV, where other processes are weak. This explains the Ca line contribution of 10.5%, which is slightly larger than the Fe contribution of 9.71%. This also emphasizes that although the absorption coefficient for an individual process may be large (greater than 10 cm^{-1}) over a wide region of the spectrum, it will not result in a large sensitivity in Table 4 if it overlaps with another process of similar or greater strength. This is because once a spectral region is completely opti-

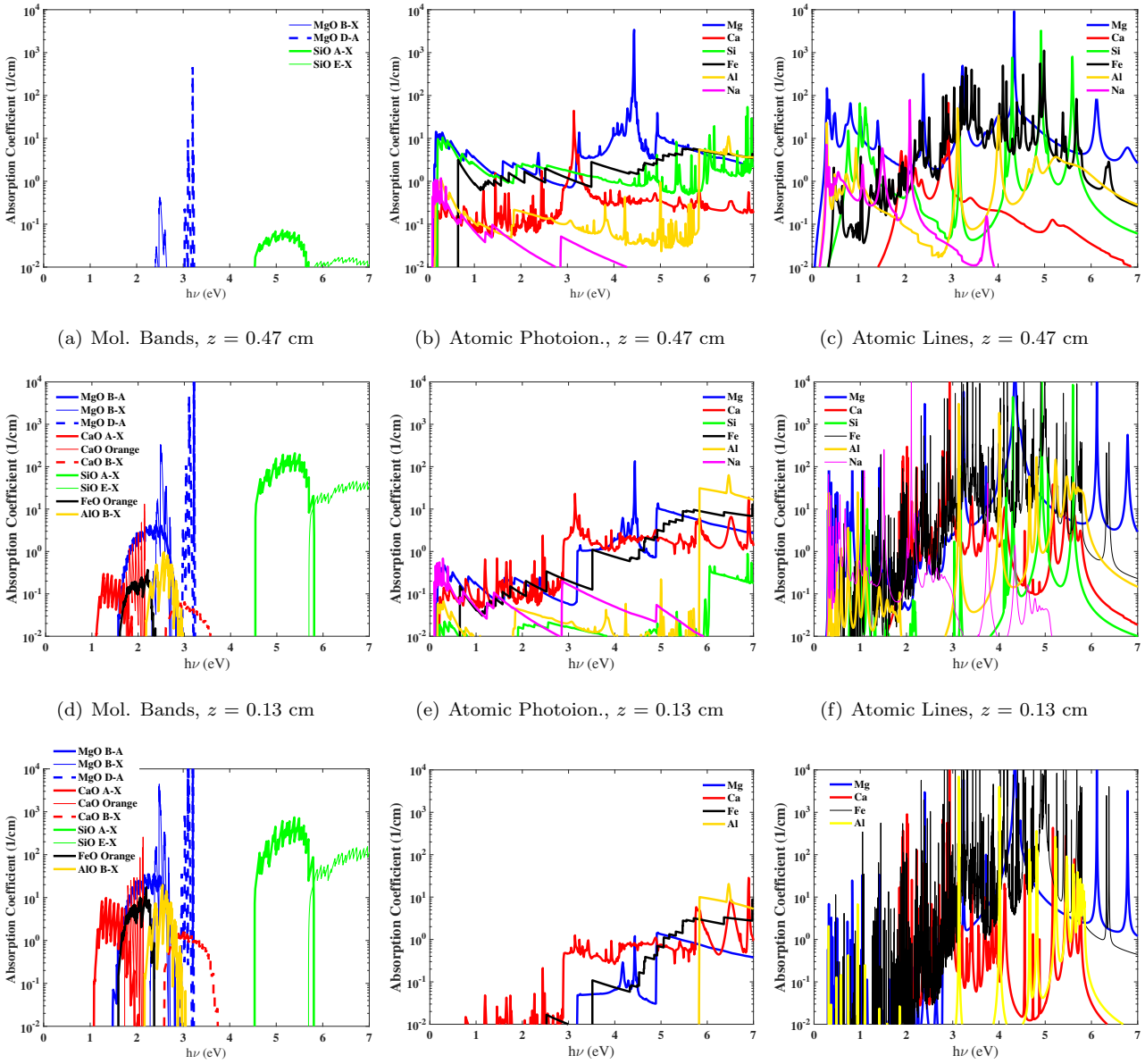

(a) Mol. Bands, $z = 0.47$ cm (b) Atomic Photoion., $z = 0.47$ cm (c) Atomic Lines, $z = 0.47$ cm

(d) Mol. Bands, $z = 0.13$ cm (e) Atomic Photoion., $z = 0.13$ cm (f) Atomic Lines, $z = 0.13$ cm

(g) Mol. Bands, $z = 0$ cm (h) Atomic Photoion., $z = 0$ cm (i) Atomic Lines, $z = 0$ cm

Figure 9: Spectrum components from individual species and radiative processes for the 30 km altitude case.

Table 4: Percent increase in stagnation point radiative flux due to removing individual radiative processes.

Specie	Mechanism	30 km	50 km
Fe	Lines	9.71	4.11
Mg	Lines	22.5	32.1
Si	Lines	1.58	1.27
Ca	Lines	10.5	5.62
Fe	Photoionization	1.75	2.51
Mg	Photoionization	3.60	6.41
Si	Photoionization	0.71	1.27
Al	Photoionization	0.16	0.32
Ca	Photoionization	1.61	3.53
Na	Photoionization	0.64	1.10
MgO	B-A	22.9	25.1
MgO	D-A	1.25	1.00
MgO	B-X	2.10	0.56
SiO	A-X	0.65	0.14
FeO	Orange	2.78	2.30
AlO	B-X	1.51	2.76
CaO	A-X	10.1	25.4
CaO	Orange	2.22	1.43

cally thick, meaning $q^-_{rad,\nu}$ is equal to the local Planck function, increasing the absorption coefficient further does not change $q^-_{rad,\nu}$.

To investigate the impact of coupled ablation on the lower pressure case at 50 km altitude, Fig. 10 compares the stagnation line temperatures and q^-_{rad} values for the coupled ablation and no ablation cases. Also presented are the ablation product mole fractions, which are only available for the coupled ablation case. Unlike for the 30 km case, where the shock stand-off increased by 25% with coupled ablation, the shock stand-off is seen to increase by over 100% for this
480 case. This difference is due to the stagnation point ablation rate being 5.1% of the free-stream mass flux for the 30 km case, while it is 51% of the free-stream mass flux for this 50 km case (even though the dimensional ablation rate is 40% lower for the 50 km case, the free-stream density is 18 times lower). The ablation product mole fractions indicate that the ablation layer extends roughly 27 cm away from the body, which causes the significant increase in the shock

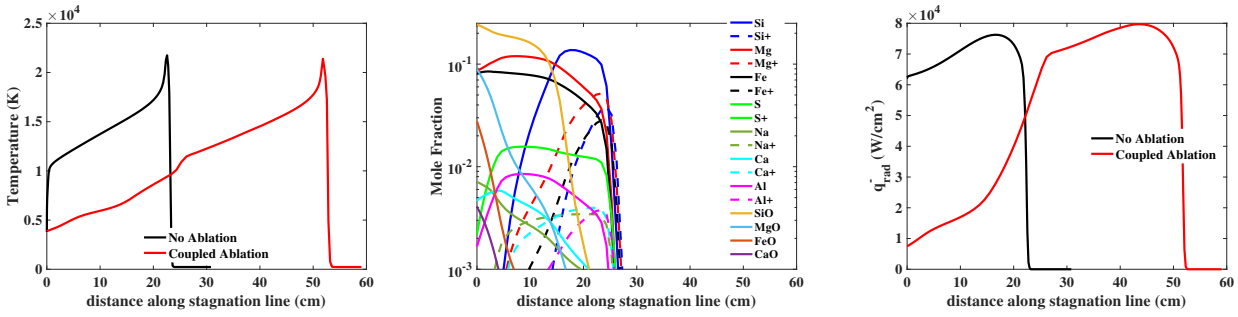

(a) (b) (c)

Figure 10: Impact of coupled ablation for the 50 km altitude case.

standoff distance. Absorption from this ablation layer reduce the q_{rad}^{-} value at the surface by 88%.

To provide further details of this 88% reduction, Fig. 11 presents the radiative flux and absorption coefficient spectra at four locations along the stagnation line. Starting at the edge of the ablation layer at 27.1 cm, which contains essentially all air species, much of the q_{rad}^{-} spectrum is seen to remain below the local Planck function (represented by the dashed line). This was shown previously in Fig. 2 for the no-ablation case. Although the temperature is 11,680 K for this point, which is higher than the other three points considered, the resulting absorption coefficient spectrum is significantly lower above 1 eV than the other points. This is a consequence of the 27.1 cm point containing all air species. This is confirmed by next considering the 22.5 cm point, which is dominated by atomic ablation species. The absorption coefficient increases by more than an order of magnitude over most of the spectrum, which drives the q_{rad}^{-} spectrum closer to the local Planck function. The individual components of the absorption coefficient are presented in Fig. 12(a) - (c) for this point. Atomic lines and photoionization from Mg and Si are dominant below 2 eV, while above this other atoms contribute noticeably. As shown in Fig. 10, the region of the ablation layer dominated by atomic species ranges from 10 to 27 cm, while molecular species dominate closer to the wall. The 4.6 cm point shown in

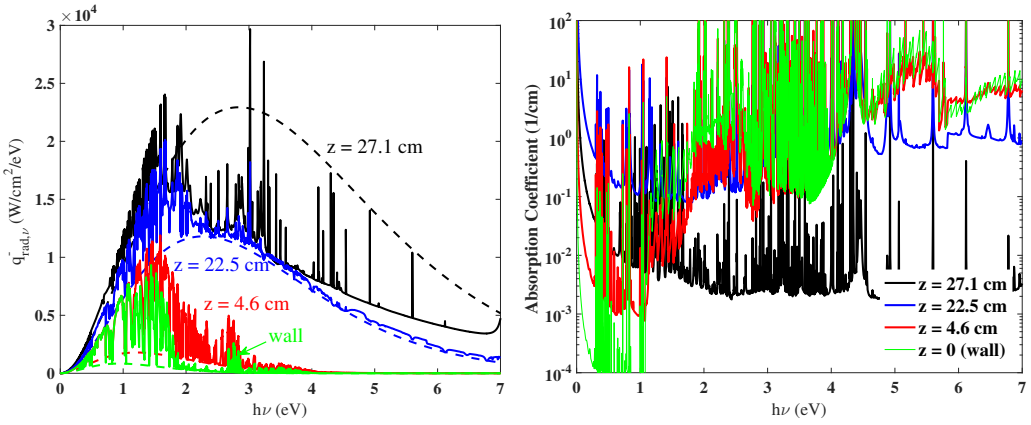

(a) (b)

Figure 11: Spectral details at various points along the stagnation line for the 50 km altitude case.

Fig. 11 represents this molecular dominated region. The significantly reduced atomic line and photoionization contributions result in decreased absorption coefficients below 2 eV. Figures 12(d) - (f) show the details of this drop-off, which are offset slightly by the increased molecular band contribution. Note that the atomic lines shown in Fig. 12(f), which are difficult to interpret, are too narrow to provide significant absorption. Moving finally to the surface, most of the q_{rad}^{-} spectrum above 2 eV that remains at 4.6 cm is absorbed due to the MgO band systems, while between 1 and 2 eV the CaO A-X band system absorbs a noticeable amount. Below 1 eV the q_{rad}^{-} spectrum remains unchanged between 4.5 cm and the wall, due the absorption decrease in this spectral region.

To summarize the observations made in the previous paragraph, Table 4 lists the percent change in q_{rad}^{-} at the wall due to removing individual processes. The most significant processes are seen to be Mg lines, MgO B-A, and CaO A-X. Recall that these processes provide not only large absorption coefficients, but are also located in regions of the spectrum that do not overlap other strong processes. This explains the relatively small sensitivities seen for overlapping

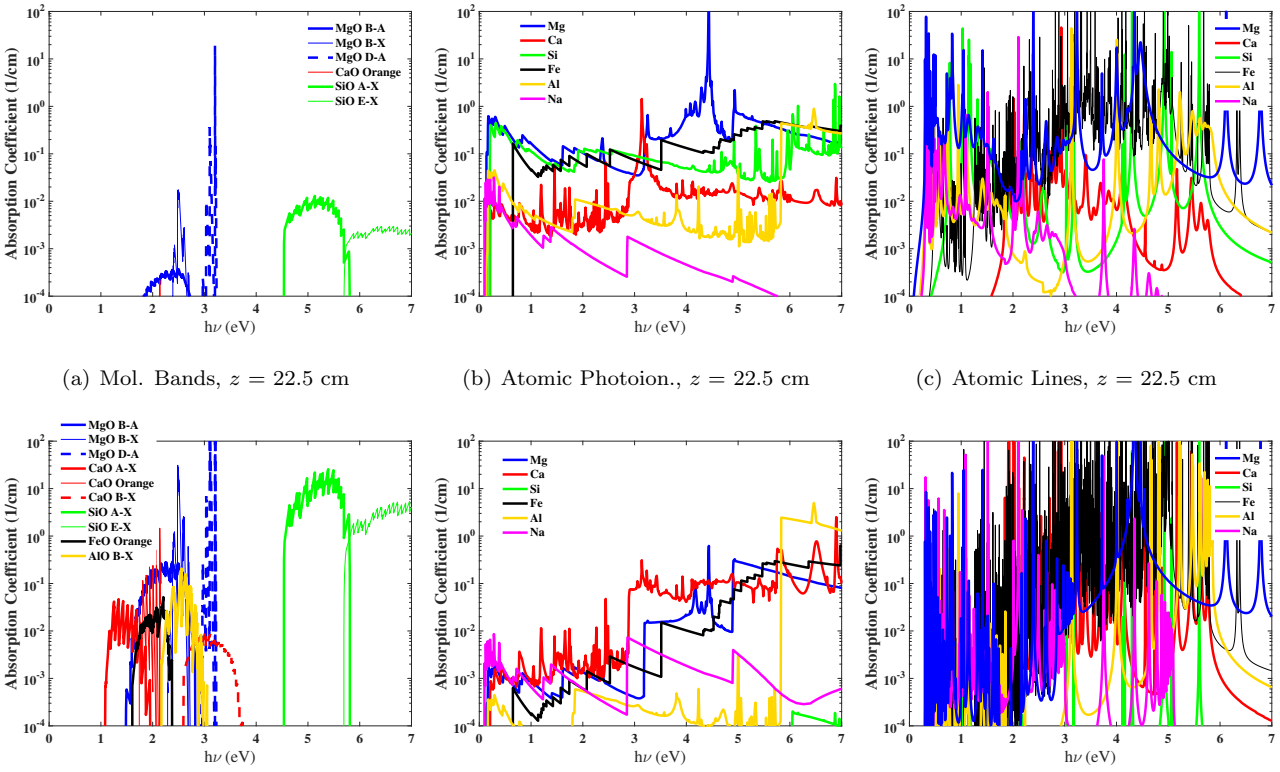

(a) Mol. Bands, $z = 22.5$ cm (b) Atomic Photoion., $z = 22.5$ cm (c) Atomic Lines, $z = 22.5$ cm

(d) Mol. Bands, $z = 4.6$ cm (e) Atomic Photoion., $z = 4.6$ cm (f) Atomic Lines, $z = 4.6$ cm

Figure 12: Spectrum components from individual species and radiative processes for the 50 km altitude case.

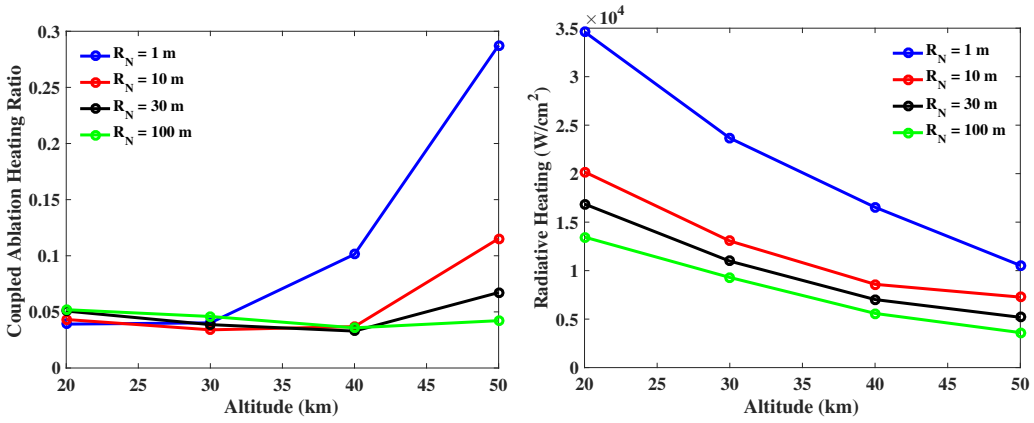

(a) (b)

Figure 13: Impact of coupled ablation on the stagnation point at 20 km/s.

photoionization processes, such as Mg, Fe, and Si, even though they contribute large absorption coefficients.

To generalize the impact of coupled ablation on the stagnation point, Fig. 13 presents the coupled ablation results for a range of nose radii and altitude, all with a velocity of 20 km/s. Figure 13(a) presents the stagnation point radiative heating with coupled ablation divided by the case with no ablation (recall that both include coupled radiation, as have all simulations presented in this section). This "coupled ablation heating ratio" is seen to remain near a value of 0.05 below 30 km, regardless of nose radius, while above 30 km the impact of coupled ablation is less (meaning the presented ratio is closer to 1) for smaller nose radii. This results from the fact that, for a given ablation rate, the ablation product layer is thicker for larger nose radii. Below 30 km this behavior is subdued because spectral regions with strong absorption are completely absorbed, resulting in the thicker absorbing ablation layer having minimal impact. Figure 13(b) presents the stagnation point radiative heating for this range of cases. Note that dividing these values by those in Fig. 4(b) will return the ratios presented in Fig. 13(a).

3.3. Impact of Turbulence

In support of the Galileo probe heatshield design for Jupiter entry, Moss et al. [69, 70] showed that turbulence had a significant impact on the radiative heating to the probe's massively ablating carbon-phenolic surface. Previous to this study, a common assumption in aerothermodynamic analyses was that turbulence had a negligible impact on radiative heating. Moss et al. showed that the higher temperatures near the surface for the turbulent case reduced the number density of the strongly absorbing C_3 molecule, which increased the radiative heating. Johnston et al. [30] found similar behavior for massively ablating Earth entry shock layers at 15 km/s. These studies suggest that turbulence will have a significant impact on the aerothermodynamic environment of a massively ablating meteor. It should also be noted that surface roughness may have a significant effect on the influence of turbulence, however, this is beyond the scope of the current work, where the intent is to provide an initial assessment of the impact of flowfield turbulence. Note that carbon is not present in the presently studied meteoroid composition, meaning that there is no C_3, which provided the primary turbulence impact in the studies by Moss et al. and Johnston et al.

The present analysis applies the Cebeci-Smith turbulence model [71, 72], with a turbulent Schmidt number of 0.9, and assumes completely turbulent flow. The presence of coupled radiation prevents the total enthalpy from being used to locate the boundary layer edge, which is required by the turbulence model. As a robust alternative, the boundary layer edge is defined as the point where the Si^+ mass fraction decreases to 5% of its peak value along a body normal line. Through trial and error, this approach was found to provide the best systematic method for locating the boundary layer edge for both mild and massive ablation rates in the presence of strong coupled radiation,. The application of this relatively simple turbulence model represents a feasible approach for assessing the impact of turbulence to the already complex coupled ablation and radiation simulations. The turbulent solutions are computed starting with

the corresponding laminar solution. The ablation rates and wall temperatures are re-converged to the turbulent heating rates.

While this paper has so far focused exclusively on the stagnation line, the present section expands the analysis to downstream locations where the impact of turbulence is more pronounced. Note that the impact of turbulence on the stagnation point is limited because the outer-layer eddy-viscosity is proportional to the boundary layer edge velocity [72], which is small for the stagnation line. A noticeable impact of turbulence is seen at the stagnation point, however, due to feedback from downstream regions (e.g., slight changes in the shock standoff distance at downstream locations impact the stagnation point shock standoff distance).

For the 30 km altitude case considered in previous sections, Fig. 14(a) compares the laminar and turbulent radiative heating values as a function of the distance along the meteoroid surface (starting from the stagnation point at 0). The vertical dotted line at 5.3 m defines the downstream location to be studied in subsequent figures. This figure shows that the turbulent radiative heating is up to 100% greater than the laminar values. Figure 14(b) shows that this increased radiative heating corresponds with a similar increase in the ablation rate.

To determine the cause of the significant increase in the radiative heating due to turbulence, Fig. 15 compares the laminar and turbulent profiles along the body normal line indicated by the dotted line in Fig. 14. The temperatures, Si and Mg mole fractions, and q_{rad}^{-} profiles between the shock and wall are presented in Figs. 15 (a) - (c). These figures show the impact of turbulence on the outer region of the boundary layer, where the atomic ablation products, such as Si and Mg, are shown to diffuse further into the shock layer. The lower temperatures for the turbulent case produce lower q_{rad}^{-} values throughout the outer region of the boundary layer (1 - 20 cm). To clarify the details below 1 cm, Figs. 15(d) - (f) focus on the first 4 cm away from the surface. The temperatures for the turbulent case are seen to become larger than the laminar values below 1 cm. These higher temperatures are seen in Fig. 15(e) to significantly reduce

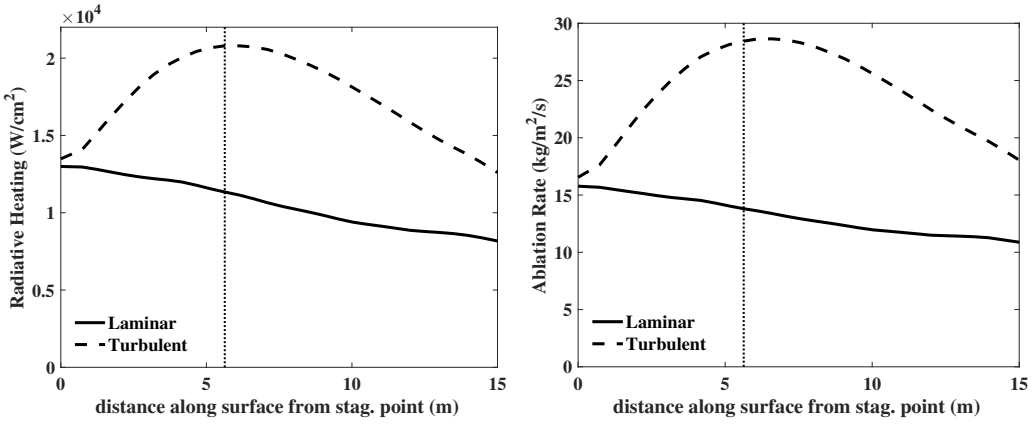

(a) (b)

Figure 14: Impact of turbulence for the 30 km altitude case.

the mole fractions of SiO and MgO. Absorption from MgO was shown in the previous subsection to provide significant absorption. The increased radiative heating for the turbulent case due to the reduction of MgO and CaO (which is not presented in the figure, but behaves similarly to MgO) is analogous to the reduction in C_3 predicted by Moss et al. for the Galileo probe.

A similar comparison is made in Figs. 16 and 17 for the lower-pressure 50 km altitude case studied in previous sections. For this case, up to a 40% increase is seen for the radiative heating and ablation rate with the addition of turbulence. Although this difference is lower than that seen for the previous higher pressure case, Fig. 17 shows that the influence of turbulence extends further into the shock layer. This is due primarily to the thicker ablation layer. As with the previous example, the temperatures for the turbulent case are higher near the surface. Again, this reduces the presence of strongly absorbing molecular species.

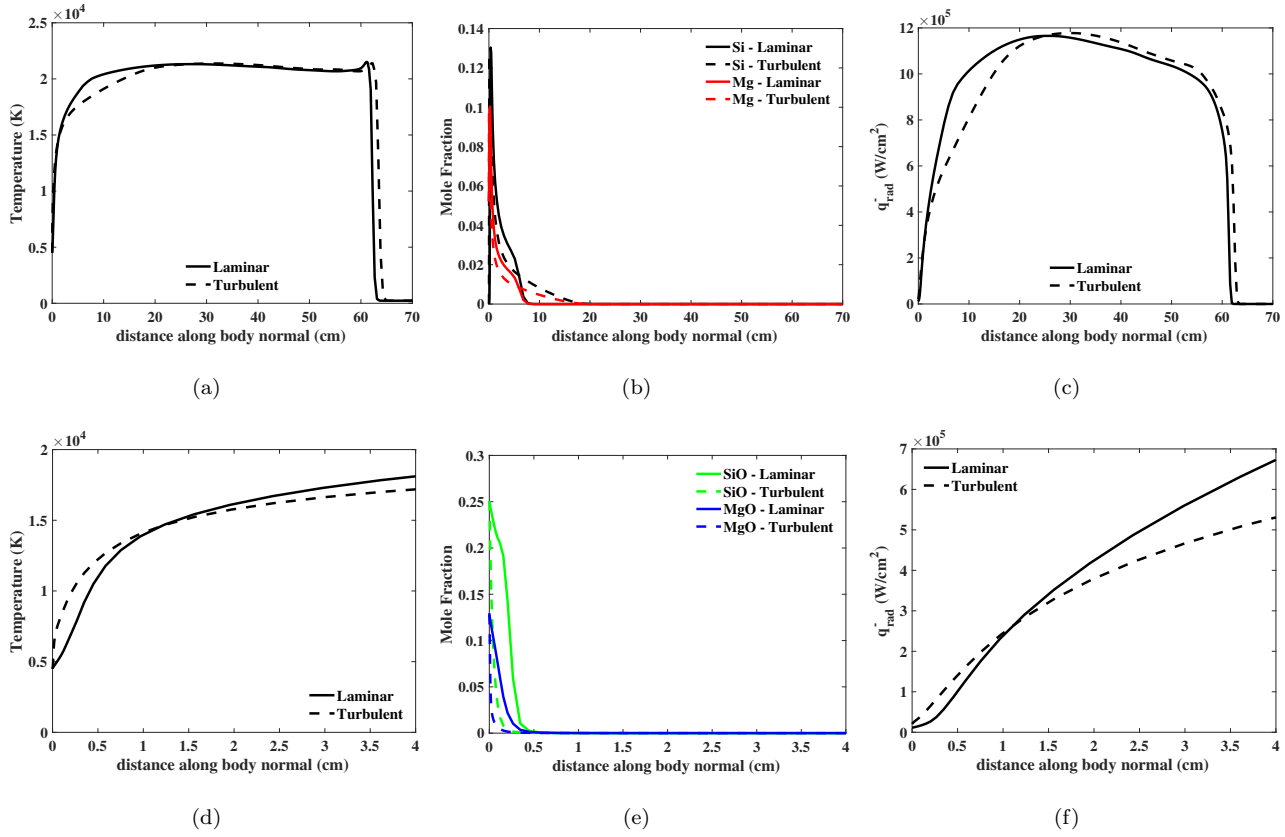

Figure 15: Impact of turbulence on the body normal line defined in Fig. 14 for the 30 km altitude case.

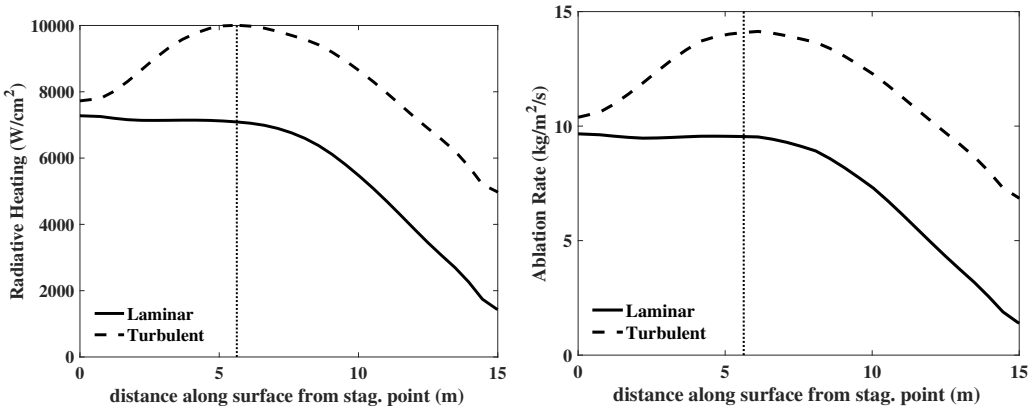

(a) (b)

Figure 16: Impact of turbulence for the 50 km altitude case.

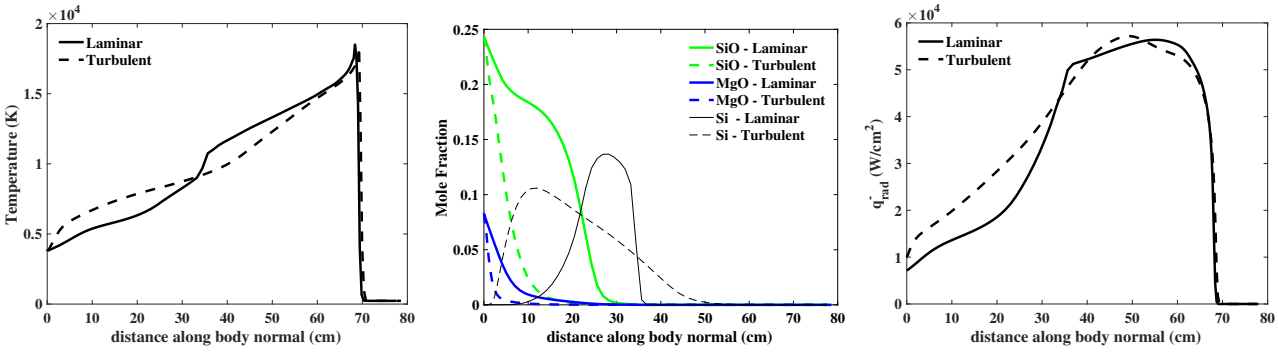

(a) (b) (c)

Figure 17: Impact of turbulence on the body normal line defined in Fig. 16 for the 50 km altitude case.

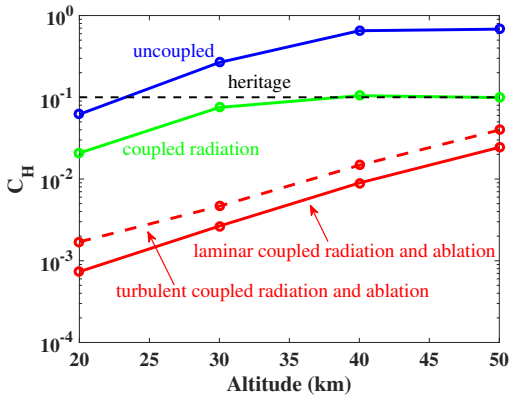

Figure 18: Impact of coupled radiation and ablation on C_H at 20 km/s and $R_N = 10$ m.

4. Heat Transfer Coefficient (C_H) Model

The previous two sections presented the impact of coupled radiation and coupled ablation on q_{rad}. Through Eq. (2), these q_{rad} values are converted to effective C_H values. For a 10 m radius meteoroid at 20 km/s, Fig. 18 provides a summary of the impact of coupled radiation, coupled ablation, and turbulence on C_H. This figure shows that, at altitudes above 30 km, coupled radiation provides C_H values similar to the heritage value of 0.1 derived by Page et al. [7, 8]. This agreement is consistent with the approach of Page et al., which included coupled radiation but not coupled ablation. Page et al. also ignored viscous effects, which are shown in the discussion of Fig. 3 to significantly reduce the radiative heating at 30 km altitude. This explains the deviation of the coupled radiation results from 0.1 at altitudes below 30 km. The most important result of Fig. 18 is the significant reduction in C_H due to coupled ablation (both with and without turbulence). This reduction in the radiative heating was discussed at length in Section 3. Again, coupled ablation was not treated in the derivation of the 0.1 value derived by Page et al.

Figure 19 presents C_H values for both laminar (solid lines) and turbulent (dashed lines) flow, which all include coupled radiation and ablation. In addition to the 20 km/s cases studied throughout this paper, simulations were also

performed for velocities of 14, 16, and 18 km/s. Although not shown, the impact of coupled radiation and ablation discussed throughout this paper is similar for these lower velocity cases. Figure 19 shows that the resulting C_H values are also similar for these lower velocities. The impact of turbulence, which is shown in the previous section to significantly impact the radiative heating, is seen to have a similar impact for the entire range of cases. However, even with turbulence, these C_H values remain considerably below the heritage value of 0.1.

Fig. 20 shows a comparison with C_H values presented by other researchers. The Park [11], Nemtchinov [73], and Biberman [29, 74] predictions all include the impact of coupled radiation and ablation. Park applied an inviscid stagnation line analysis. The stagnation-point radiative heating values presented by Park were converted to C_H values by scaling them with the present stagnation-point radiative heating and C_H values. Nemtchinov applied an ablating piston flowfield model, while Biberman applied an inviscid stagnation line analysis. Note that the Biberman values are taken from the tabulated values presented by Golub et al. [75]. Excellent agreement is seen between the present results and those of Biberman. The Park and Nemtchinov values, however, are more than a factor of two larger than the present results.

Because of the minimal details available regarding the Nemtchinov [73] and Biberman [29, 74] simulations, it is difficult to investigate further their comparison with the present results shown in Fig. 20. The study by Park [11], however, provides sufficient details to investigate its significantly higher C_H values. To see if this disagreement is due to differences in the applied elemental composition, h_{abl} curve-fit, or T_w curve-fit, simulations were performed using the Park values for these quantities. Park's values for h_{abl} are near 9 MJ/kg, compared to the values applied throughout this work, which are near 6.2 MJ/kg. These larger h_{abl} values result in smaller ablation rates through Eq. (10). For T_w, Park's values are roughly 500 K lower than the present values. Park determined these values for an H-Chondrite with the following elemental mass fractions: O = 0.352, Si = 0.194, Fe = 0.272, Mg = 0.159, S = 0.022. Note that Al, Ca, and Na are not included. These values for h_{abl}, T_w, and elemental composition were

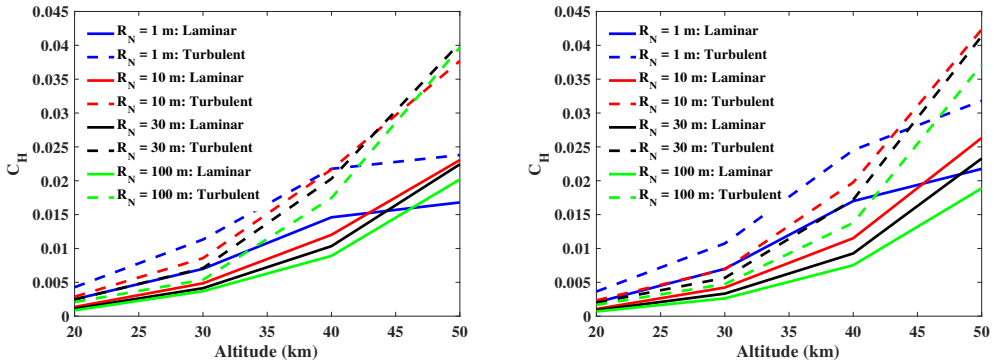

(a) 14 km/s

(b) 16 km/s

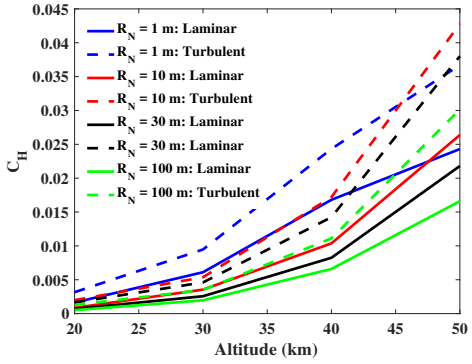

(c) 18 km/s

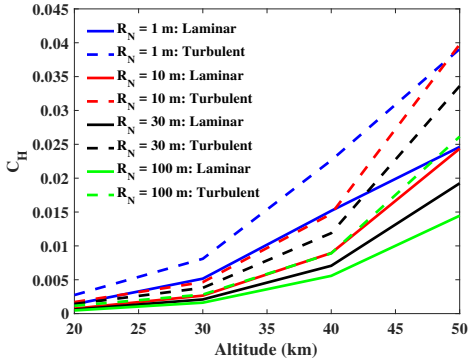

(d) 20 km/s

Figure 19: Coupled radiation and ablation C_H values for a range of velocities, altitudes, and nose radii.

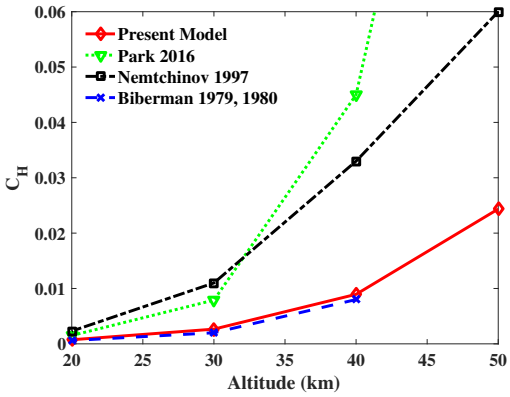

Figure 20: Comparison of C_H values at 20 km/s and $R_N = 10$ m predicted by various studies.

applied in the present simulation approach for the 30 and 50 km altitude (20 km/s and 10 m nose radius) cases studied throughout this paper. These values resulted in C_H increases of 11% and 20% for the 30 and 50 km altitude cases, respectively, relative to the present baseline model. These C_H values of 0.0028 and 0.029 for the 30 and 50 km cases remain a factor of three below the Park values (the Park value at 50 km is 0.16, which is off the scale in Fig. 20). It is concluded from this comparison that differences between the applied h_{abl}, T_w, and elemental composition values do not account for the differences between the present C_H values and those predicted by Park. This comparison also shows that the present C_H values are not overly sensitive to the meteoroid composition and ablation model.

5. Effect of Detailed C_H Model on Tunguska Airburst

Analytic models of asteroid entry and breakup are used to evaluate the potential damage and risk from asteroids striking Earth [5, 76, 4, 77, 78, 79] Such models integrate simplified meteor physics equations to assess aerodynamic breakup and estimate the energy deposited in the atmosphere through drag and ablation. These energy deposition results can then be used to estimate airburst altitudes and resulting ground damage areas in asteroid impact risk assessments [2, 80]. They can also be compared with energy deposition estimates

from observed meteor light curves in order to make inferences about the object's pre-entry properties or breakup characteristics [5, 81, 82]. To evaluate the potential effects of the present simulation-based C_H values for such applications, curve fits of the C_H results were incorporated into the Fragment-Cloud Model (FCM) [5] for comparison with heritage C_H results.

The FCM represents the breakup process using a combination of discrete fragments, and aggregate clouds of debris. The fragment components are used to represent coherent chunks that are large enough to be treated as aerodynamically independent, while the cloud components represent the remaining smaller debris that is more influenced by common group aerodynamics and can be treated as a single collective mass. The model integrates standard single-body meteor physics equations of motion and ablation [37, 83] to compute flight trajectories, velocities, and masses of the fragmenting bolide components throughout entry. The breakup process is represented as a series of progressive fragmentation events, triggered when the stagnation pressure ($\rho_\infty V_\infty^2$) exceeds the aerodynamic strength of the body, similar to the approach of ReVelle [84, 85]. Each break event splits the bolide into a given number of independent sub-fragments and a debris cloud of a specified mass-fraction. The strength of each child fragment is increased relative to its decreased size according to a Weibull-like size-strength scaling relation [86, 83], and each fragment continues independent descent until its strength is again exceeded and another break occurs, producing another set of sub-fragments and another debris cloud. Each debris cloud is modeled as a continuously dispersing, deforming mass, that quickly broadens and decelerates under a common bow shock, following the approach of Hills and Goda [4]. The descent of each fragment and cloud is integrated until it has fully ablated or reaches the ground. The energy deposited in the atmosphere through drag and ablation is then computed as the change in kinetic energy of all fragments and clouds per unit of altitude. Details of the FCM approach, flight integration equations, and energy deposition results are presented in Wheeler et al. [5], and its risk assessment applications are presented in Mathias et al. [2].

At each integration step, the ablation mass loss is computed according to Eq. (1), which requires C_H. To conveniently apply the new C_H model, the values from Fig. 19 were curve-fit. For the laminar results, the resulting curve-fit is:

$$C_{H,Lam} = \frac{1.107 \times 10^{-3}}{V_\infty R_N^{0.22}} exp\left(-8.5818 \times 10^{-4} h_{alt}^2 + 0.1753 h_{alt}\right) \quad (11)$$

and for the turbulent results the curve-fit is (note the exponent on V_∞):

$$C_{H,Turb} = \frac{0.03612}{V_\infty^{1.5} R_N^{0.22}} exp\left(1.3411 \times 10^{-4} h_{alt}^2 + 0.09694 h_{alt}\right) \quad (12)$$

These curve fits are used to compute specific C_H values for each fragment and cloud component at each integration step, given its current altitude (h_{alt}), velocity (V_∞), and frontal radius (R_N). The ablation mass loss is then computed from Eq. (1) using the variable C_H value and a constant $Q = 8.26 \times 10^6$ J/kg. For velocity, radius, and altitude values outside the bounds of the curve fit, the inputs are restricted to its valid ranges (10 m $\leq R \leq$ 100 m, 14 km/s $\leq V_\infty \leq$ 20 km/s, and $h_{alt} \geq$ 20 km). For altitudes above 50 km, C_H is capped at 0.04.

As an ablation comparison test case, FCM was used to model a Tunguska-like 15 Mt impact case both with a constant heritage C_H of 0.1, and using variable C_H values from the curve fit of the laminar simulation results. The impact energy, initial diameter, entry velocity, entry angles, and aerodynamic breakup strength for the test case were chosen based on values used in the stone-type Tunguska cases presented in Chyba et al. [76]. A higher density of 5480 kg/m^3 was used to maintain the 15 Mt impact energy and 29 m radius with the spherical bolide assumption used in FCM (vs. the 3500 kg/m^3 density used to produce equivalent mass with the cylindrical bolide shape used the Chyba model). The aerodynamic breakup pressure was set to 23.5 MPa in FCM, which yields a stagnation pressure breakup condition ($\rho_\infty V_\infty^2 > 23.5$ MPa) equivalent to the Chyba model's breakup condition (central pressure of $1.7\rho_\infty V_\infty^2/4 > 10$ MPa). The FCM model was run using a 50% cloud mass fraction and with a strength scaling exponent of 0.1, which are representative of parameter values used for stony-type impactors in FCM risk assessment applications [2].

Fig. 21 shows comparisons of the resulting FCM energy deposition curves using the simulation-based laminar C_H values vs. the heritage value of 0.1. The lower simulation-based C_H values result in less mass ablation throughout the entry, causing more mass to persist longer and pushing the energy deposition flare profile downward by several kilometers.

Table 5 gives a comparison of the airburst altitudes, resulting blast damage radii, and energy of the remaining mass impacting the ground from the energy deposition results in Fig. 21. Airburst altitudes can be estimated from the altitude at which half of the initial energy has been deposited and blast damage areas are taken as the area within which the blast overpressure on the ground exceeds 4 psi [4]. The 4-psi ground damage radius is computed based on height-of-burst energy-scaling of nuclear test data, as formulated by Hills and Goda [4, 87].

For this test case, burst altitude estimates decreased by up to 2.1 km (by over 18%), compared to those produced from the heritage C_H value. While the burst altitude differences may seem relatively small (and are within uncertainty ranges of the broader entry modeling problem), they increase blast damage radius estimates by up to three times and increase damage areas by up to nearly 10 times. The actual damage increase may be even larger since, at these low altitudes, the momentum associated with the entry increases the damage beyond what is estimated using the approach of Hills and Goda [88]. The lower ablation rates also cause significantly more mass to survive entry, increasing the amount of energy directly impacting the surface by orders of magnitude.

Although not presented here, additional test cases were also run using a range of fragmentation parameters, lower strengths (1-10 MPa) and densities (2500 kg/m^3) representative of more recent estimates for stony asteroids [89], and larger diameter (100 m). Generally, the trends remain similar to the test case presented here, with the simulation-based C_H values decreasing burst altitude results by around 1.5-3.3 km (5-35% lower) for Tunguska-scale impacts, and by up to 5 km lower (4-40% lower) for larger 100 m diameter cases. Cases were also run using a curve fit of the turbulent C_H simulation values, but the results

Table 5: Comparison of airburst altitudes, 4-psi blast damage radii, and surface-impacting energy from the Tunguska-like FCM cases. Airbursts are estimated from the altitude at which half of the initial energy has been deposited.

	Burst Altitude (km)		Blast Radius (km)		Surface Energy (kt)	
Entry Angle	C_H fit	$C_H = 0.1$	C_H fit	$C_H = 0.1$	C_H fit	$C_H = 0.1$
15°	14.4	15.4	4.8	1.5	3.4	0.2
30°	12.5	14.0	10.2	6.3	2.4	0.2
45°	11.0	12.8	13.5	9.6	5.5	0.7
90°	9.1	11.2	16.5	13.1	18.8	0.3

were nearly identical to those using the laminar values. Both the laminar and turbulent values are low enough that drag and velocity dominate the energy deposition during breakup.

6. Conclusions

A coupled radiation and ablation model is developed, that treats 39 flowfield species, to investigate the aerothermodynamics of atmospheric entry for large meteoroids. This detailed model includes species containing Fe, Mg, Si, Ca, Na, S, and Al. Radiation models for these atomic species, as well as their associated molecules are developed and implemented. Precursor absorption and photochemistry is included in this model, and is shown to have a negligible impact on heating below 40 km. The impact of coupled radiation is shown to reduce the radiative heating by more than 60% for meteor entries at 20 km/s with nose radii between 1 and 100 m and altitudes between 20 and 50 km. The impact of coupled radiation for optically thick shock layers, which occur below 40 km, is shown to produce two distinct layers of strong coupling near the shock and wall, which appear similar to a nonequilibrium post shock region and a large boundary layer, respectively. For the considered range of conditions, coupled ablation is shown to reduce the radiative heating by more than 70%. Absorption from Mg and MgO, along with Ca and CaO, are shown to have the largest impact on the radiative heating. Turbulence is shown to reduce the

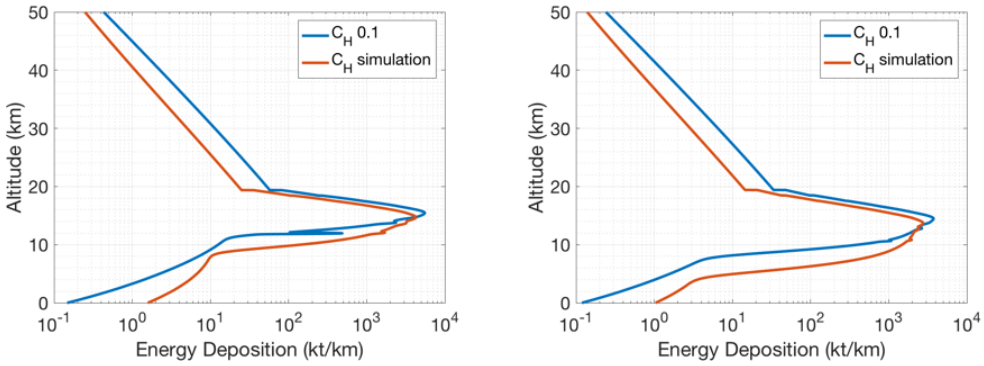

(a) 15° Entry Angle

(b) 30° Entry Angle

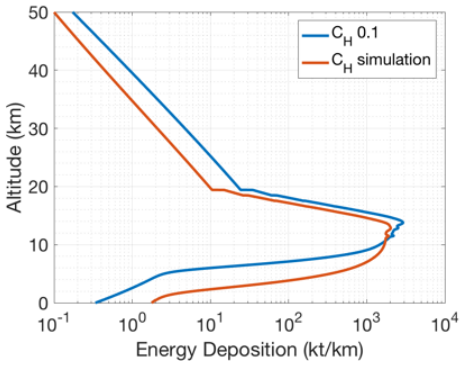

(c) 45° Entry Angle

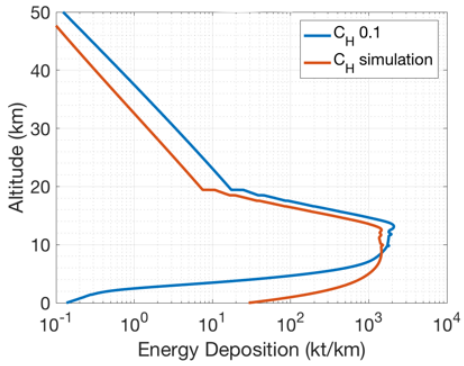

(d) 90° Entry Angle

Figure 21: Comparison of FCM energy deposition results for a Tunguska-like 15 Mt impact case modeled at four entry angles using simulation-based C_H values (red) vs. a nominal $C_H = 0.1$ (blue).

number density of strongly absorbing molecules near the surface, which is shown to result in up to a 100% increase in the radiative heating downstream of the stagnation point. Heat transfer coefficients, C_H, that include coupled radiation and ablation are computed for velocities ranging from 14 to 20 km/s, nose radii between 1 and 100 m, and altitudes between 20 and 50 km. These C_H values are lower than 0.045 for all cases, which is significantly lower than the typically assumed value of 0.1. Incorporating these lower C_H values into analytic models of asteroid entry and breakup is shown to reduce the resulting airburst altitude estimates and increase damage area estimates for impact risk assessments.

References

[1] M. Aftosmis, M. Nemec, D. L. Mathias, M. J. Berger, Numerical simulation of bolide entry with ground footprint prediction, AIAA Paper 2016–0998 (2016).

[2] D. L. Mathias, L. F. Wheeler, J. L. Dotson, A probabilistic asteroid impact risk model: assessment of sub-300m impacts, Icarus 289 (2017) 106–119.

[3] D. O. Revelle, Recent Advances in Bolide Entry Modeling: A Bolide Potpourri, Earth 95 (1) (2004) 441–476.

[4] J. G. Hills, M. P. Goda, The fragmentation of small asteroids in the atmosphere, Astronomical Journal (ISSN 0004-6256) 105 (1993) 1114–1144.

[5] L. F. Wheeler, P. J. Register, D. L. Mathias, A fragment-cloud model for asteroid breakup and atmospheric energy deposition, Icarus 295 (2017) 149–169.

[6] D. K. Prabhu, D. Saunders, P. Agrawal, Thermophysics issues relevant to high-speed earth entry of large asteroids, AIAA Presentation, (https://ntrs.nasa.gov/search.jsp?R=20160000692) (2016).

[7] W. A. Page, D. L. Compton, W. J. Borucki, D. L. Ciffone, D. M. Cooper, Radiative transport in inviscid nonadiabatic stagnation-region shock layers, AIAA Paper 68–784 (1968).

[8] B. Baldwin, Y. Sheaffer, Ablation and breakup of large meteoroids during atmospheric entry, Journal of Geophysical Research 76 (1971) 4653–4666.

[9] C. O. Johnston, J. Samareh, A. M. Brandis, Aerothermodynamic characteristics of 16-22 km/s earth entry, AIAA Paper 2015–3110 (2016).

[10] C. O. Johnston, P. A. Gnoffo, K. Sutton, Influence of ablation on radiative heating for earth entry, Journal of Spacecraft & Rockets 46 (3) (2009) 481–491.

[11] C. Park, Inviscid-flow approximation of radiative ablation of asteroidal meteoroids by line-by-line method, AIAA Paper 2016–0506 (2016).

[12] B. Dias, A. Turchi, T. Magin, Stagnation-line simulations of meteor ablation, AIAA Paper 2015–2349 (2015).

[13] A. Mazaheri, P. A. Gnoffo, C. O. Johnston, B. Kleb, Laura users manual, NASA TM 2010-216836 (2010).

[14] B. J. Mcbride, M. J. Zehe, S. Gordon, Nasa glenn code for calculating coefficients for calculating thermodynamic properties of individual species, NASA TP 2002–211556 (2002).

[15] M. J. Wright, D. Bose, G. Palmer, E. Levin, Recommended collision integrals for transport property computations 1: Air species, AIAA Journal 43 (12) (2005) 2558–2564.

[16] M. J. Wright, H. Hwang, D. W. Schwenke, Recommended collision integrals for transport property computations part 2: Mars and venus entries, AIAA Journal 45 (1) (2007) 281–288.

[17] R. A. Svhehla, Estimated viscosities and thermal conductivities of gases at high temperatures, NASA TR R 142 (1962).

[18] C. Park, R. L. Jaffe, H. Partridge, Chemical-kinetic parameters of hyperbolic earth entry, Journal of Thermophysics and Heat Transfer 15 (1) (2001) 76–90.

[19] C. O. Johnston, P. A. Gnoffo, A. Mazaheri, Influence of coupled radiation and ablation on the aerothermodynamic environment of planetary entry vehicles, VKI Lecture STO-AVT-218 (2013).

[20] C. O. Johnston, B. R. Hollis, K. Sutton, Spectrum modeling for air shock-layer radiation at lunar-return conditions, Journal of Spacecraft & Rockets 45 (2008) 865–878.

[21] C. O. Johnston, B. Hollis, K. Sutton, Non-boltzmann modeling for air shock layers at lunar return conditions, Journal of Spacecraft & Rockets 45 (2008) 879–890.

[22] C. O. Johnston, A. M. Brandis, D. Bose, Radiative heating uncertainty for hyperbolic earth entry, part 3: Comparisons with east measurements, Journal of Spacecraft & Rockets 50 (1) (2013) 48–55.

[23] C. O. Johnston, K. Sutton, D. Prabhu, D. Bose, Radiative heating uncertainty for hyperbolic earth entry, part 2: Comparisons with 1960s era shock tube measurements, Journal of Spacecraft & Rockets 50 (1) (2013) 39–47.

[24] A. M. Brandis, C. O. Johnston, B. A. Cruden, D. K. Prabhu, D. Bose, Validation of high speed earth atmospheric entry radiative heating from 9.5 to 15.5 km/s, AIAA Paper 2012–2865 (2012).

[25] P. A. Gnoffo, C. O. Johnston, R. A. Thompson, Implementation of radiation, ablation, and free-energy minimization in hypersonic simulations, Journal of Spacecraft & Rockets 47 (2) (2010) 481–491.

[26] C. O. Johnston, A. Mazaheri, Impact of non-tangent-slab radiative transport on flowfield-radiation coupling, AIAA Paper 2017–1371 (2017).

[27] R. Goulard, The coupling of radiation and convection in detached shock layers, Journal of Quantitative Spectroscopy and Radiative Transfer 1 (1961) 249–257.

[28] R. Goulard, Preliminary estimates of radiative transfer effects on detached shock layers, AIAA Journal 2 (3) (1964) 494–502.

[29] L. M. Biberman, S. Y. Ronin, M. V. Brykin, Moving of a blunt body through the dense atmosphere under conditions of severe aerodynamic heating and ablation, Acta Astronautica 7 (1) (1980) 53–65.

[30] C. O. Johnston, A. Mazaheri, P. Gnoffo, B. Kleb, D. Bose, Radiative heating uncertainty for hyperbolic earth entry, part 1: Flight simulation modeling and uncertainty, Journal of Spacecraft & Rockets 50 (1) (2013) 19–38.

[31] S. A. Stanley, L. A. Carlson, Effects of shock wave precursor ahead of hypersonic entry vehicles, Journal of Spacecraft & Rockets 29 (2) (1992) 190–197.

[32] A. K. Mnatsakanyan, Photodissociation and photoionization of diatomic molecules at high temperatures, High Temperature 6 (1968) 230–235.

[33] G. S. Romanov, Y. A. Stankevich, L. K. Stanchits, K. L. Stepanov, Thermodynamic and optical properties of gases in a wide range of parameters, International Journal of Heat and Mass Transfer 38 (3) (1995) 545–556.

[34] W. Cunto, C. Mendoza, F. Ochsenbein, C. Zeippen, Topbase at the cds, Astronomy and Astrophysics 275 (1993) L5–L8, see also vizier.u-strasbg.fr/topbase/topbase.html.

[35] P. A. Gnoffo, R. N. Gupta, J. L. Shinn, Conservation equations and physical models for hypersonic air flows in thermal and chemical nonequilibrium, NASA TP 2867 (Feb. 1989).

[36] Y.-K. Chen, Thermal ablation modeling for silicate materials, AIAA Paper 2016–1514 (2016).

[37] E. J. Öpik, Physics of meteor flight in the atmosphere., Dover Publications, Inc., New York, 1958.

[38] S. Gordon, B. J. Mcbride, Thermodynamic data to 20,000 k for monatomic gases, NASA TP 1999–208523 (1999).

[39] C. Park, J. T. Howe, R. L. Jaffe, G. V. Candler, Review of chemical-kinetic problems for future nasa missions, ii: Mars entries, Journal of Thermophysics and Heat Transfer 8 (1) (1994) 9–23.

[40] H.-J. Mick, M. Burmeister, P. Roth, Atomic resonance absorption spectroscopy measurements on high-temperature co dissociation kinetics, AIAA Journal 31 (4) (1993) 671–676.

[41] S. D. L. Picard, A. Canosa, D. Reignier, T. Stoecklin, A comparative study of the reactivity of the silicon atom si towards o_2 and no molecules at very low temperatures, Physical Chemistry Chemical Physics 4 (2002) 3659–3664.

[42] U. S. Akhmadov, I. S. Zaslonko, V. N. Smirnov, Mechanism and kinetics of interaction of fe, cr, mo, and mn, Kinetics and Catalysis 29.

[43] A. Hodgson, J. Mackie, A shock tube study of the kinetics of evaporation and oxidation of magnesium, Combustion and Flames 35.

[44] C. W. Lu, Y. J. Wu, Y. P. Lee, R. S. Zhu, M. C. Lin, Experiments and calculations on rate coefficients for pyrolysis of so_2 and the reaction o plus so at high temperatures, Journal of Physical Chemistry A 107 (2002) 11020–11029.

[45] Y. Murakami, S. Onishi, T. Kobayashi, N. Fujii, N. Isshiki, K. Tsuchiya, A. Tezaki, H. Matsui, High temperature reaction of s+so_2 = so+so: Implication of s_2o_2, Journal of Physical Chemistry A 107 (2003) 10996 – 11000.

[46] N. L. Garland, Temperature dependence of the reaction: So + o_2, Chemical Physics Letters 290 (1998) 385 – 390.

[47] N. Cohen, K. R. Westberg, Chemical kinetic data sheets for high-temperature chemical reactions, Journal of Physical and Chemical Reference Data 12.

[48] A. Fontijn, W. Felder, Htffr kinetics studies of the al/so_2 reaction from 700 to 1600 k. implications for d(al-o), Journal of Chemical Physics 71.

[49] J. M. C. Plane, D. Husain, Determination of the absolute rate constant for the reaction o+nao = na+o_2 by time-resolved atomic chemiluminescence, J. Chem. Soc. Faraday Trans. 2 82 (1986) 2047 – 2052.

[50] O. E. Kashireninov, V. A. Kuznetsov, G. B. Manelis, Kinetics of alkaline-earth atoms reactions with molecular oxygen, AIAA Journal 15 (1977) 1035 – 1037.

[51] H. R. Griem, Spectral Line Broadening by Plasmas, Academic Press, New York, 1974.

[52] C. Park, Rosseland mean opacities of air and h-chondrite vapor in meteor entry problems, Journal of Quantitative Spectroscopy and Radiative Transfer 127 (2013) 158–164.

[53] M. Geier, C. B. Dreyer, T. E. Parker, Laser-induced emission spectrum from high-temperature silica-generating flames, Journal of Quantitative Spectroscopy and Radiative Transfer 109 (2008) 822–830.

[54] C. Park, J. O. Arnold, A shock-tube determination of the sio ($a^1\pi - x^1\sigma^+$) transition moment, Journal of Quantitative Spectroscopy and Radiative Transfer 19 (1978) 1–10.

[55] G. T. Naidu, R. R. Reddy, T. V. R. Rao, r-centroids and franck-condon factors of the sio molecule, Physica C 106 (1981) 308–310.

[56] I. Drira, A. Spielfiedel, S. Edwards, N. Feautrier, Theoretical study of the $a^1\pi - x^1\sigma^+$ and $e^1\sigma^+ - x^1\sigma^+$ bands of sio, Journal of Quantitative Spectroscopy and Radiative Transfer 60 (1998) 1–8.

[57] A. Lagerqvist, I. Renhorn, N. Elander, The spectrum of sio in the vacuum ultraviolet region, Journal of Molecular Spectroscopy 46 (1973) 285–315.

[58] H. H. Michels, Theoretical determination of metal oxide f numbers, AFWL-TR 74-239 (1975).

[59] J. W. Daily, C. Drewer, A. Abbud-Madrid, M. C. Branch, Transition probabilities in the $b^1\sigma^+ - a^1\pi$ electronic systems of mgo, Journal of Molecular Spectroscopy 214 (2002) 111–116.

[60] R. A. Bell, P. H. Dwivedi, D. Branch, J. N. Huffaker, Rotational dependence of franck-condon factors for selected band systems of tio, zro, mgo, lao, and sio, Astrophysical Journal Supplement Series 41 (1979) 593–630.

[61] C. Naulin, M. Costes, Z. Moudden, G. Dorthe, Measurements of the radiative lifetimes of mgo (b,d,d) states, Chemical Physics Letters 2 (1991) 325–329.

[62] P. H. Doherty, A. J. Midey, T. M. Miller, D. J. Levandier, E. Holeman, D. F. Webb, K. Martin, Comprehensive methods for determining space effects on air force systems, AFRL-RV-HA-TR 2009-1100 (2009).

[63] H. S. Liszt, W. H. Smith, Rkr franck-condon factors for blue and ultraviolet transitions of some metal oxides, Journal of Quantitative Spectroscopy and Radiative Transfer 11 (1971) 1043–1062.

[64] L. Pasternack, P. J. Dagdigian, The reaction of metastable ca atoms with o_2 and co_2, Chemical Physics 33 (1978) 1–11.

[65] D. P. Baldwin, R. W. Field, The green-band transitions of cao, Journal of Molecular Spectroscopy 139 (1990) 68–76.

[66] A. C. Borin, F. R. Ornellas, A theoretical investigation of the $a^3\pi$-$x^3\sigma^-$ transition in so, Chemical Physics Letter 322 (2000) 149–156.

[67] B. Rosen, Spectroscopic Data Relative to Diatomic Molecules, Pergamon Press, 1970.

[68] J. Borovicka, A. A. Berezhnoy, Radiation of molecules in benesov bolide spectra, Icarus 278 (2016) 248–265.

[69] J. N. Moss, A. L. Simmonds, Galileo probe forebody flowfield predictions during jupiter entry, AIAA Paper 1982–0874 (1982).

[70] J. N. Moss, A. L. Simmonds, E. C. Anderson, Turbulent radiating shock layers with coupled ablation injection, Journal of Spacecraft & Rockets 17 (3) (1980) 177–183.

[71] T. Cebeci, Variation of the van driest damping parameter with mass transfer, AIAA Journal 11 (2) (1973) 237–238.

[72] F. M. Cheatwood, R. A. Thompson, The addition of algebraic turbulence modeling to program laura, NASA TM 107758 (1993).

[73] I. V. Nemtchinov, V. V. Svetsov, I. B. Kosarev, A. P. Golub, O. P. Popova, V. V. Shuvalov, Assessment of kinetic energy of meteoroids detected by satellite-based light sensors, Icarus 130 (1997) 259–274.

[74] L. M. Biberman, S. Y. Bronin, M. V. Brykin, Heat transfer in hypersonic flow with strong radiative convective interaction, High Temperature 17 (1979) 84–91.

[75] A. P. Golub, I. B. Kosarev, I. V. Nemchinov, V. V. Shuvalov, Emission and ablation of a large meteoroid in the course of its motion through the earth's atmosphere, Solar System Research 30 (3) (1996) 213–228.

[76] C. F. Chyba, P. J. Thomas, K. J. Zahnle, The 1908 Tunguska Explosion - Atmospheric Disruption of a Stony Asteroid, Nature 361 (6407) (1993) 40–44.

[77] G. S. Collins, H. J. Melosh, R. A. Marcus, Earth Impact Effects Program: A Web-based computer program for calculating the regional environmental consequences of a meteoroid impact on Earth, Meteoritics & Planetary Science 40 (6) (2005) 817–840.

[78] C. Rumpf, H. G. Lewis, P. M. Atkinson, On the influence of impact effect modelling for global asteroid impact risk distribution, Acta Astronautica 123 (C) (2016) 165–170.

[79] G. H. Stokes, D. K. Yeomans, W. F. Bottke, S. R. Chesley, Study to determine the feasibility of extending the search for near-Earth objects to smaller limiting diameters, Tech. rep. (2003).

[80] S. Motiwala, D. Mathias, C. Mattenberger, An Integrated Physics-Based Risk Model for Assessing the Asteroid Threat, in: International Topical Meeting on Probabilistic Safety Assessment and Analysis, 2015, pp. 1–20.

[81] P. J. Register, D. L. Mathias, L. F. Wheeler, Asteroid fragmentation approaches for modeling atmospheric energy deposition, Icarus 284 (C) (2017) 157–166.

[82] P. G. Brown, D. O. Revelle, E. Tagliaferri, An entry model for the Tagish Lake fireball using seismic, satellite and infrasound records, Meteoritics & Planetary Science 37 (5) (2002) 661–675.

[83] V. A. Bronshten, Physics of Meteoric Phenomena, Springer, 1983.

[84] D. O. Revelle, Recent Advances in Bolide Entry Modeling: A Bolide Potpourri, Earth, Moon, and Planets 95 (1) (2004) 441–476.

[85] D. O. Revelle, NEO fireball diversity: energetics-based entry modeling and analysis techniques, Proceedings of the International Astronomical Union 2 (S236) (2007) 95–12.

[86] W. Weibull, A Statistical Theory of the Strength of Materials, Proc. Royal Swedish Academy. Eng. Sci. (1939).

[87] S. Glasstone, P. J. Dolan, The Effects of Nuclear Weapons, U.S. Government Printing Office, 1977.

[88] M. Boslough, D. A. Crawford, Low-altitude airbursts and the impact threat, International Journal of Impact Engineering 35 (12) (2008) 1441–1448.

[89] O. Popova, J. Borovička, W. K. Hartmann, P. Spurný, E. Gnos, I. Nemtchinov, J. M. Trigo-Rodriguez, Very low strengths of interplanetary meteoroids and small asteroids, Meteoritics & Planetary Science 46 (10) (2011) 1525–1550.